Kent Academic Repository
Full text document (pdf)

Citation for published version

DOI

Link to record in KAR

Document Version

Author's Accepted Manuscript

A population of hypercompact H II regions identified from young H II regions

A. Y. Yang[1], J. S. Urquhart[2], M. A. Thompson[3], K. M. Menten[1], F. Wyrowski[1], A. Brunthaler[1], W. W. Tian[4,5], M. Rugel[1], X. L. Yang[6], S. Yao[6], M. Mutale[3]

[1] Max Planck Institute for Radio Astronomy, Auf dem Hügel 69, 53121, Bonn, Germany
e-mail: ayyang@mpifr-bonn.mpg.de
[2] Centre for Astrophysics and Planetary Science, University of Kent, Canterbury, CT2 7NH, UK

[3] Centre for Astrophysics Research, School of Physics Astronomy & Mathematics, University of Hertfordshire, College Lane, Hatfield, AL10 9AB, UK

[4] CAS Key Laboratory of FAST, National Astronomical Observatories, Chinese Academy of Sciences, Beijing, 100012

[5] University of Chinese Academy of Sciences, 19A Yuquan Road, Shijingshan District, Beijing 100049, China

[6] Kavli Institute for Astronomy and Astrophysics, Peking University, Beijing 100871, China

ABSTRACT

Context. The derived physical parameters for young H II regions are normally determined assuming the emission region to be optically-thin. However, this is unlikely to hold for young H II regions such as Hyper-compact H II (HC H II) and Ultra-compact H II (UC H II) regions and leads to the underestimation of their properties. This can be overcome by fitting the SEDs over a wide range of radio frequencies.
Aims. Two primary goals are (1) determining physical properties from radio SEDs and finding potential HC H II regions; (2) using these physical properties to investigate their evolution.
Methods. We used Karl G. Jansky Very Large Array (VLA) to make observations of X-band and K-band with angular-resolutions of $\sim 1.7''$ and $\sim 0.7''$, respectively, toward 114 H II regions with rising-spectra ($\alpha_{1.4\,\mathrm{GHz}}^{5\,\mathrm{GHz}} > 0$). We complement our observations with VLA archival data and construct SEDs between $1-26$ GHz and model them assuming an ionisation-bounded H II region with uniform density.
Results. The sample has a mean electron density of $n_e = 1.6 \times 10^4\,\mathrm{cm}^{-3}$, diameter *diam* = 0.14 pc, and emission measure EM = $1.9 \times 10^7\,\mathrm{pc\,cm}^{-6}$. We identify 16 HC H II region candidates and 8 intermediate objects between the classes of HC H II and UC H II regions. The n_e, *diam*, and EM change as expected, however, the Lyman continuum flux is relatively constant over time. We find that about 67% of Lyman continuum photons are absorbed by dust within these H II regions and the dust absorption fraction tends to be more significant for more compact and younger H II regions.
Conclusions. Young H II regions are commonly located in dusty clumps; HC H II regions and intermediate objects are often associated with various masers, outflows, broad radio recombination lines, and extended green objects, and the accretion at the two stages tends to be quickly reduced or halted.

Key words. ISM: H II regions –ISM: evolution–radio continuum: stars–stars: massive–stars: formation

1. Introduction

One key question in the massive star formation related to the youngest H II region is that how does accretion proceed against the outward pressure of the H II region (e.g., Keto & Wood 2006), as massive stars reach the main sequence while still accreting (e.g., Zinnecker & Yorke 2007; Motte et al. 2018). However, many details of the earliest stage of H II regions are unclear. Simple analytic models suggest that the H II region can be created either by the ionized, inner part of the inflowing material (Keto 2002, 2003) or the ionized photoevaporative outflow (Hollenbach et al. 1994) fed by accretion (Keto 2007). The onset time for a H II region is thought to be developed early in the McKee & Tan (2003) and Peters et al. (2010) turbulent core and ioniza-

tion feedback models but is suggested to be delayed in the models of Hosokawa & Omukai (2009) and Hosokawa et al. (2010) for a bloated protostar. After the birth of H II regions, the subsequent expansion has been modeled as uniform spherical bubbles (Spitzer 1978), or asymmetrical flows into outflow-driven cavities (Peters et al. 2010), and the expansion rate predicted by different models could also be different (e.g., Bisbas et al. 2015). Detailed observations toward the youngest H II regions are crucial to investigate their initial development and constrain the theoretical models (Thompson et al. 2015, 2016).

The two youngest H II region stages are commonly known as hyper-compact H II (HC H II) and ultra-compact H II (UC H II) regions (e.g., Kurtz 2005). The youngest is the HC H II region with typical physical size *diam* $\lesssim$ 0.05 pc, electron density

$n_e \gtrsim 10^5 \, \text{cm}^{-3}$, emission measure EM $\gtrsim 10^8 \, \text{pc} \, \text{cm}^{-6}$, and line width of radio recombination line (RRL) $\Delta V \gtrsim 40 \, \text{km} \, \text{s}^{-1}$ (Kurtz et al. 2000; Sewilo et al. 2004; Hoare et al. 2007; Murphy et al. 2010). The ultra-compact H II (UC H II) region is thought to be the next evolutionary stage after the HC H II region, with typical *diam* $\lesssim 0.1 \, \text{pc}$, $n_e \gtrsim 10^4 \, \text{cm}^{-3}$, EM $\gtrsim 10^7 \, \text{pc} \, \text{cm}^{-6}$, and $\Delta V \sim 25 - 30 \, \text{km} \, \text{s}^{-1}$ (e.g., Wood & Churchwell 1989; Afflerbach et al. 1996; Hoare et al. 2007). The defining characteristics of these two stages (i.e., size, electron density, and emission measure) are somewhat arbitrary, as the evolution from HC H II regions to UC H II regions is thought to be continuous (e.g., Garay & Lizano 1999; Yang et al. 2019). Compared to the hitherto discovered ~ 600 UC H II regions (Urquhart et al. 2007, 2009b; Lumsden et al. 2013; Urquhart et al. 2013; Cesaroni et al. 2015; Kalcheva et al. 2018; Djordjevic et al. 2019), only sixteen HC H II regions have been identified in previous studies (summarised by Yang et al. 2019 and references therein). It is not yet clear at what stage and how an HC H II region evolves into an UC H II region. Given the fact that the observed sizes of young H II regions are found to vary with the observing frequency (Panagia & Felli 1975; Avalos et al. 2006), the classical quantitative criteria for identifying HC H II regions are suggested to be modified in order to consider the variations (Yang et al. 2019), which could lead to a better understanding of the intermediate object between an HC H II region and an UC H II region. However, to understand the relation between the two classes, and eventually to understand the early stages of newly-formed massive stars, reliable properties toward a large sample of young H II regions including HC H II regions and UC H II regions are needed to be determined.

These young H II regions around massive stars are heavily obscured by the thick cocoon of molecular gas, however, they can be studied at radio wavelengths due to the ability of radio radiation to penetrate the dense molecular gas. Therefore, most studies of young H II regions are based on radio continuum observations (e.g., Wood & Churchwell 1989; Kurtz et al. 1994; van der Tak & Menten 2005; Gibb & Hoare 2007). The radio continuum spectrum of an H II region with spectral index α ($S_\nu \propto \nu^\alpha$) varies from +2 (optically thick) at low frequency to −0.1 (optically thin) at high frequency. The turnover frequency between the optically thick and thin regimes for thermal bremsstrahlung is essentially a linear function of the electron density (Mezger & Henderson 1967). A younger H II region with higher density will remain optically thick at higher frequencies. For instance, UC H II regions have a typical turnover frequency of $\nu_t \sim 5 \, \text{GHz}$, while HC H II regions have $\nu_t = 10$ to $100 \, \text{GHz}$ (e.g., Beltrán et al. 2007; Hoare et al. 2007; Keto et al. 2008; Zhang et al. 2014). Therefore, young H II regions with spectra still rising in a higher frequency are potentially young and dense, which might correspond to an early stage of UC H II region or a stage connecting UC H II and HC H II regions.

The physical properties of young H II regions have been measured in several previous studies (e.g., Wood & Churchwell 1989; Murphy et al. 2010; Urquhart et al. 2013; Kalcheva et al. 2018; Medina et al. 2019), either by a targeted multi-band observation on small samples of UC H II regions (e.g., Murphy et al. 2010) or by using single-band surveys assuming that the gas is optically thin to free-free emission (e.g., Urquhart et al. 2013; Kalcheva et al. 2018). The assumption that H II regions are optically thin would give unreliable physical properties if the H II region is actually optically thick at the observed frequency. Therefore, multi-band data taken over a large range of frequencies is crucial to obtain reliable properties for young H II regions.

Table 1. The observed 114 rising spectra H II regions. Column 1 gives source name, in Cols. 2 and 3 give the flux density at 1.4 GHz and 5 GHz respectively (see Yang et al. (2019) for details), Cols. 4-6 give the heliocentric distance and bolometric luminosity and the reference these values are drawn from. The uncertainties for the fluxes and distances are estimated to be 10%, and the 20% for the luminosity.

Name	$S_{1.4\,GHz}$ (mJy)	$S_{5\,GHz}$ (mJy)	Dist (kpc)	L_{bol} ($L_\odot$)	[Ref.]
	(2)	(3)	(4)	(5)	(6)
G010.3009−00.1477	426.2	631.4	3.5	5.2	[1]
G010.4724+00.0275	31.3	38.4	8.5	5.7	[1]
G010.6223−00.3788†	327.6	483.3	2.4	5.7	[1]
G010.6234−00.3837	571.3	1952.2	5.0	5.7	[1]
G010.9584+00.0221	47.9	196.0	2.9	4.0	[1]
G027.9782+00.0789	89.3	124.0	4.8	4.2	[2]
G028.2003−00.0494	–	161.0	6.1	5.1	[1]
G028.2879−00.3641	410.9	552.8	11.6	5.9	[1]
G028.6082+00.0185	168.2	210.2	7.4	5.0	[1]
G029.9559−00.0168	1610.8	3116.2	5.2	5.7	[1]
G049.3704−00.3012	252.9	414.4	5.4	5.1	[3]
G048.6099+00.0270	56.5	131.2	9.8	5.1	[4]

Notes. Only a small portion of the data is provided here, the full table is presented in Table A.1 and will be available in electronic form at the CDS. Source names appended with a † refers to the sources observed that could not be imaged. References: [1] Urquhart et al. (2018), [2] Cesaroni et al. (2015), [3] Urquhart et al. (2013), [4] Kalcheva et al. (2018).

In this work, we report on the results of multi-band observations with the Karl G. Jansky Very Large Array[1] (VLA) in X-band (8–12 GHz) and K-band (18–26 GHz) of a sample of 114 young H II regions. These sources were selected from a sample of H II regions with rising spectra between 1.4 GHz and 5 GHz, i.e., $\alpha_{1.4\,\text{GHz}}^{5\,\text{GHz}} > 0$ (Yang et al. 2019). Together with archival VLA data at 1.4 GHz and 5 GHz (see Sect. 2.1 for details), we measure the spectral energy distribution (SED) between 1–26 GHz for each source in the sample, which covers both optically thick and thin portions of their radio spectra. We model every SED to find the best estimates for the physical properties.

This paper is organized as follows: Section 2 describes the details of the sample, observation, and data reduction. Section 3 presents and discusses the observational results, the modeled SEDs, and the sources' radio properties and its distributions. In Section 4, we discuss HC H II region candidates, plus a small sample of objects considered to be in an intermediate phase between HC H II and UC H II regions. We use our observations to derive the physical properties (electron densities, diameter, emission measure, Lyman continuum flux) of H II regions and compare our multi-band results to those estimated using the optically thin assumption. In Section 5 we discuss the relations and distribution of all of the UC H II and HC H II regions. We present a summary of this work and highlight our conclusions in Section 6.

2. Observation

2.1. Sample selection

In Yang et al. (2019), we constructed a parent sample of 534 objects with rising radio spectral indexes between 1.4 GHz and 5 GHz using three JVLA surveys, THOR (The HI, OH, Recombination line survey of the Milky Way, Bihr et al. 2016; Beuther

---

[1] The Karl G. Jansky Very Large Array of the National Radio Astronomy Observatory: https://science.nrao.edu/facilities/vla

Table 2. Summary of VLA observation parameters.

Parameter	
Project	VLA18B-065
Frequency (GHz)	X-band (8 − 12) & K-band(18–26)
Array configuration	C
Observing mode	continuum
Bandwidth per channel	128 MHz
No. Channels	30 & 60
Primary beam	∼ 4.2′ & ∼ 1.9′
Synthesized beam	∼ 2.0″ × 1.4″ & ∼ 0.7″ × 0.6″
Observing dates	2019 Feb 07 & 2019 Feb 26
Time on-source per source	∼ 1 min
No. Targets	114
Total observing time	2h & 2.5h
Flux density calibrator (Jy)	3C286 (4.5 Jy)
Phase calibrators (Jy)	J1832-1035 (1.28 Jy)
	J1851-0035 (1.10 Jy)
	J1922+1530 (1.0 Jy)

et al. 2016), MAGPIS (The Multi-Array Galactic Plane Imaging Survey, White et al. 2005; Helfand et al. 2006), and COR-NISH (Coordinated Radio "N" Infrared Survey for High-mass star formation, Hoare et al. 2012; Purcell et al. 2013). From an analysis of the combined radio, infrared, and submillimetre emission properties (Yang et al. 2019), we identified 120 young H II regions from the parent sample. This sample not only recovers previously known HC H II regions, but also includes broad radio recombination line (RRL) objects with line widths of $\Delta V > 40 \, \mathrm{km \, s^{-1}}$ and a number of UC H II regions with positive spectra (Yang et al. 2019). We have observed 114 young H II regions in X- and K-band data taken with the VLA. We use the data from archive and literature for the 4 sources in the initial sample that haven't been observed in the project, marked ⋆ in Table 1 and Table 7. The final sample includes 118 young H II regions.

The flux densities and angular diameters of the 118 observed sources are given in Table 1. The 1.4 and 5 GHz flux densities are taken from Yang et al. (2019) and references therein. The distances and bolometric luminosities are mainly drawn from the results reported in Urquhart et al. (2018) [2], which includes 105 objects of the sample. For the remaining 13 sources with no measurements in Urquhart et al. (2018), their distances and bolometric luminosities are taken from three studies such as Cesaroni et al. (2015), Urquhart et al. (2013), and Kalcheva et al. (2018). The kinematic distances were computed by fitting the radial velocity of each source to the Galactic rotation curve. The kinematic distances near/far ambiguity (KDA) for sources within the solar circle were resolved by CO emission line data and H I absorption (e.g., Urquhart et al. 2013; Cesaroni et al. 2015; Kalcheva et al. 2018) or by using a combination of H I analysis, maser parallax and spectroscopic measurements (Urquhart et al. 2018). The bolometric luminosity of the sample was taken from the same reference as the distance and was determined by integrating the SED from near-infrared to submillimeter wavelengths (e.g., König et al. 2017).

---

[2] This study by Urquhart et al. (2018) is based on the ATLASGAL compact source catalog, which consists of ∼10 000 clumps showing submillimeter wavelength emission from dust (Contreras et al. 2013; Urquhart et al. 2014).

2.2. VLA observations and data reduction

The observations of 114 young H II regions were carried out using the VLA in C configuration. The instrument parameters for the VLA observation are shown in Table 2. The observations were made at X-band (8–12 GHz) and K-band (18–26 GHz), which is split into two subbands with 30 channels at X-band, and four subbands with 60 channels at K-band, each channel with a bandwidth of 128 MHz, full stokes. The synthesized beams in C configuration at X-band and K-band are ∼ 1.8″ and ∼ 0.7″, and the FWHM primary beams sizes are ∼ 4.2′ and ∼ 2′, respectively. The typical on-source time for each target is about one minute and the total observation time is 4.5 hours. The phase calibrators (J1832-1035, J1851-0035, and J1922+1530) were observed every half hour at X-band and every twelve minutes at K-band to correct the amplitude and phase of the interferometer data by atmospheric and instrumental effects. The pointing corrections at the high-frequency K-band were determined by observing the nearby phase calibrators in interferometric pointing mode. The absolute flux density scale at X-band and K-band was calibrated by comparing the observations of the standard flux density scale calibrator J1331+305 (3C286) with its models provided by the NRAO.

Standard calibration and data reduction were performed using the Common Astronomy Software Applications package (CASA, McMullin et al. 2007). Raw VLA data were calibrated and reduced by running the CASA pipeline. We discarded the first 3 s of data of every scan for calibrators to exclude the antenna settling time. Flux and phase calibrator data were carefully examined to ensure high-quality data. A calibration table was produced and applied to all targeted data. Each target was inspected by eye to flag bad data such as phase scatters, errant amplitudes, system-temperature spikes, which resulted in a mean on-source integration time ∼ 50 s for each source.

Images were constructed using the default Briggs robust parameter of zero, which gives a good trade-off between the low thermal noise of natural weighting and the high resolution of uniform weighting. Due to short on-source time (∼50 s), we adopt frequency ranges as wide as possible for each image to do the `clean` task in CASA. In order to measure flux density at different frequencies, we produced multi-band images at X-band and K-band. At X-band, three images were produced at central frequencies of 9 GHz (8–10 GHz), 10 GHz (8–12 GHz), and 11 GHz (10–12 GHz). Also, at K-band, three images were produced at central frequencies of 20 GHz (18–22 GHz), 22 GHz (18–26 GHz), and 24 GHz (22–26 GHz). The final beam size of images at the central frequency of X-band 10 GHz and the central frequency of K-band 22 GHz are ∼ 2.1″ × 1.4″ and ∼ 0.7″ × 0.6″. Sources with $\theta < 1.8″$ (X-band) and $\theta < 0.8″$ (K-band) are considered to be unresolved. Sources with angular size $\theta > 1.8″$ (X-band) and $\theta > 0.8″$ (K-band) are considered to be resolved and the deconvolved sizes are given in Table 3.

3. Results and Analysis

3.1. Observational results

In Fig. 1, we present images of three sources that show the typical variation in emission structure observed in our sample. The contour levels shown in these images were determined using a dynamic range power-law fitting scheme to meaningfully represent both high and low dynamic range images (e.g., Thompson et al. 2006; Urquhart et al. 2009b; Yang et al. 2018). This has been slightly altered from the scheme described by Thompson
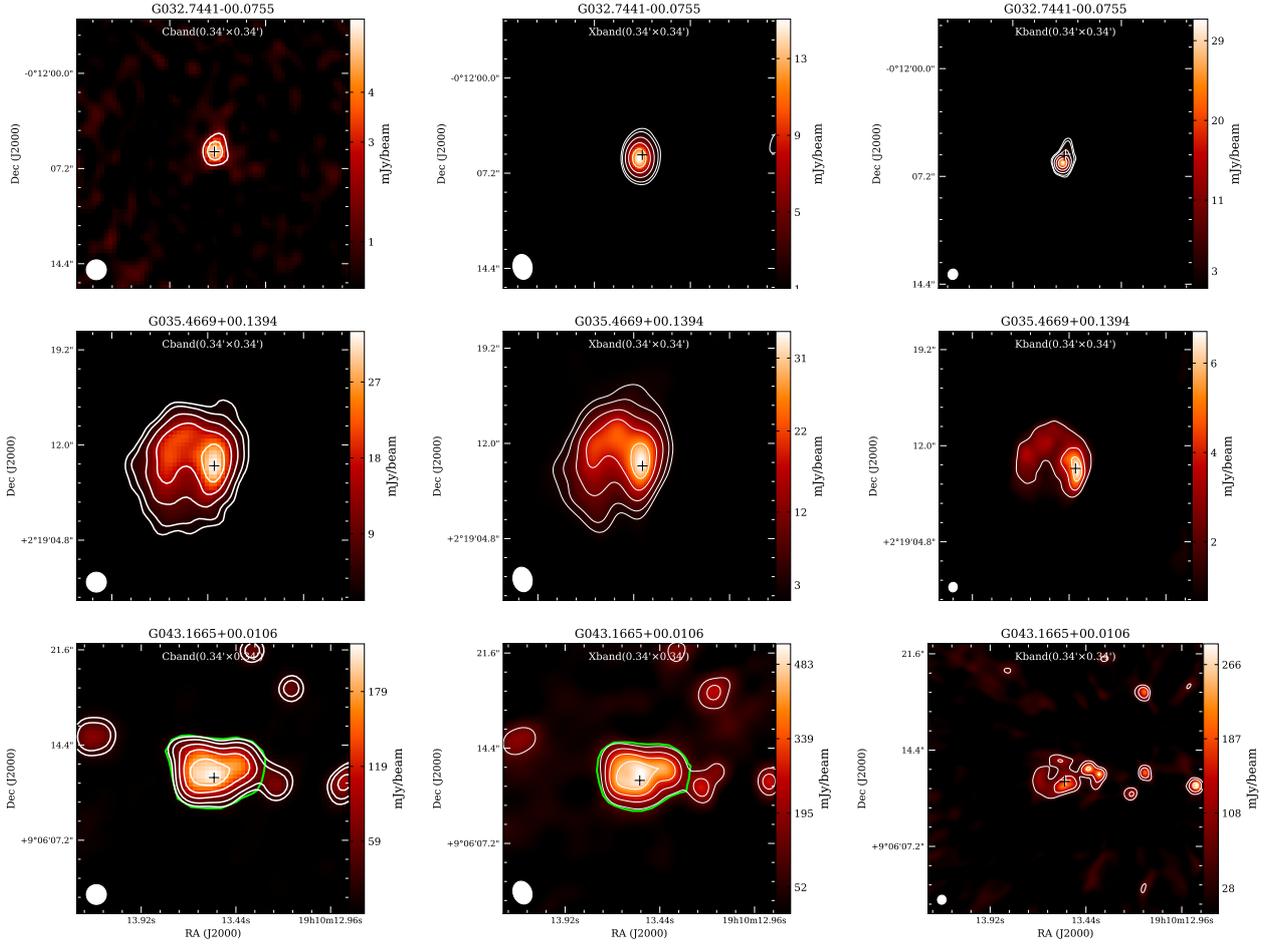
Fig. 1. Example images of three radio sources at C-band (left-column), X-band (middle-column), and K-band (right-column). The position of the H ɪɪ region is marked with a plus. In the upper, middle, and lower rows, we show the maps for the compact H ɪɪ region G032.7441−00.0755, the extended H ɪɪ region G035.4669+00.1394 and the H ɪɪ region G043.1665+00.0106 located in a cluster (see Sect. 3.1), respectively. C-band images have been taken from the CORNISH survey. The white contour levels of each image are equally spaced by 5σ and starting at a level of 5σ. The green outline shown in the lower row shows the polygon that was manually drawn round to the H ɪɪ region located in a cluster. The image size and beam size are shown in the upper-middle and lower-left of each image. The C-band, X-band, and K-band images for the whole sample are shown in Appendix Figure B.1 and will be available in electronic form at the CDS.

Table 3. Observational results of 112 young H ɪɪ regions at X-band (8–12 GHz) and K-band (18–26 GHz). Columns: (1) Source name; (2) and (3) peak flux density and local RMS at X-band; (4-6) flux density at 9 GHz, 10 GHz and 11 GHz, respectively; (7) deconvolved source size at X-band; (8) and (9) peak flux density and RMS at K-band; (10-12) flux density at 20 GHz, 22 GHz, and 24 GHz, respectively; (13) deconvolved source size at K-band. The uncertainties in the flux measurements are estimated to be 10%.

Source name	$S_{Peak}(X)$ (mJy/beam)	$\sigma(X)$ (mJy)	$S_{9\,GHz}$ (mJy)	$S_{10\,GHz}$ (mJy)	$S_{11\,GHz}$ (mJy)	$\theta_s(X)$ ($''\times''$)	$S_{Peak}(K)$ (mJy/beam)	$\sigma(K)$ (mJy)	$S_{20\,GHz}$ (mJy)	$S_{22\,GHz}$ (mJy)	$S_{24\,GHz}$ (mJy)	$\theta_s(K)$ ($''\times''$)
(1)	(2)	(3)	(4)	(5)	(6)	(7)	(8)	(9)	(10)	(11)	(12)	(13)
G010.3009−00.1477⊕	88.1	3.1	700.3	686.7	661.4	6.8×6.6	15.9	0.7	433.4	419.6	392.6	6.5×6.4
G010.4724+00.0275	82.5	1.6	100.7	105.9	115.4	1.4×0.4	66.9	0.8	156.8	159.9	172.0	1.6×0.5
G010.6234−00.3837⊕	1099.9	7.9	3071.4	3072.1	3314.8	4.2×3.8	572.3	14.6	2884.8	2857.2	2851.5	3.1×3.0
G010.9584+00.0221	186.3	1.5	258.3	256.2	265.0	1.2×0.9	91.3	1.2	210.7	202.6	200.6	1.0×0.7
G011.0328+00.0274	3.9	0.2	4.8	4.3	4.1	1.3×0.9	1.7	0.1	3.4	2.9	2.8	0.9×0.4
G011.1104−00.3985⊕	70.5	0.7	350.4	334.8	327.7	9.5×9.4	15.6	0.4	136.1	123.3	126.1	2.2×1.7
G011.1712−00.0662⊕	4.1	0.1	95.1	92.7	100.1	11.9×8.6	0.6	0.1	-	-	-	−
...	...	...	...									
G011.9368−00.6158⊕	306.7	2.0	1116.4	1083.5	1098.3	3.4×3.2	76.4	2.0	656.1	652.4	629.6	2.8×1.8
G011.9446−00.0369⊕	85.7	2.0	709.6	691.4	724.6	6.3×4.7	20.0	0.6	307.2	291.6	289.9	4.3×2.1
G012.1988−00.0345	29.6	0.4	66.0	64.8	63.9	2.0×1.9	6.5	0.2	59.6	54.7	55.9	2.0×2.0
G012.2081−00.1019	88.0	0.8	212.5	209.3	206.5	2.3×1.9	27.2	0.6	159.0	142.1	140.8	2.0×1.2

Notes. ⊕ indicates the sources are extended and their K-band flux densities should be considered to be lower limits. Only a small portion of the data is provided here, the full table is shown in Table A.2 and will be available in electronic form at the CDS. † refers to the added 5 UC H ɪɪ regions with rising spectra between C and X band, see Sect 3.1.
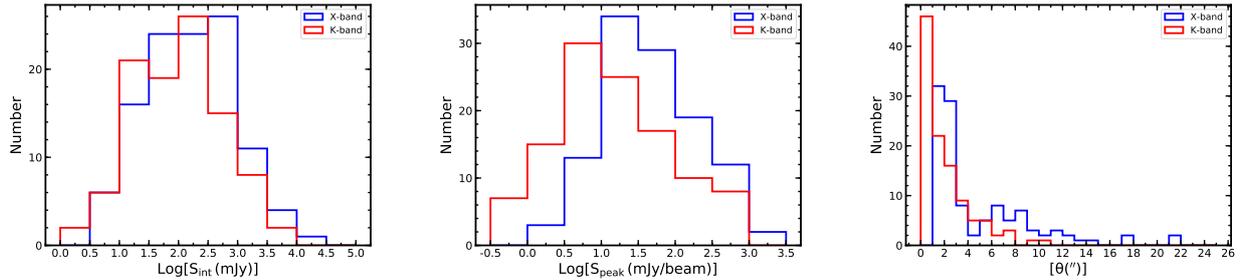
Fig. 2. Distributions of observation results such as integrated flux density S_{int}, peak flux density S_{peak}, and angular size θ, of 116 young H II regions at X-band (blue solid line) and K-band (red solid line). The bin sizes are 0.5 dex, 0.5 dex, 1″ for S_{int}, S_{peak}, and θ, respectively.

et al. (2006) and can be described as the following relationship $D = 5 \times N_i + 5$, where D is the dynamic range of the map (defined as the ratio between the peak brightness and the 1σ RMS noise), N is the number of contour lines, and i is the contour power-law index. Here, the minimum power-law index was one, which resulted in linearly spaced contours starting at 5σ and increasing in steps of 5σ. The starting contour level we adopted for each target is variable, ranging from 5σ to 7σ according to the RMS level of each image. The RMS noise level (σ) of each image was determined by using the standard deviation (STDEV = $1.4826 \times$ MADFM), where MADFM is the median absolute deviation from the median (MADFM = median($|X_i - $ median$(X)|$ (where X is one element in the data set), to reduce the effects of outliers on noise measurement (e.g., Purcell et al. 2013). The short on-source integration time of the target observation (~ 50 s) could lead to a rather high RMS level on the observed field for some sources located in complex star formation regions.

The compact sources in the sample are directly fitted by 2D Gaussian models using the `imfit` task in CASA (see upper panels of Fig. 1). The resolved UC H II regions are classified into a variety of morphologies ranging from spherical to irregular (e.g. Wood & Churchwell 1989; Urquhart et al. 2007, 2009b, 2013; Purcell et al. 2013). The properties of the extended sources (see the middle row of Fig. 1) and UC H II regions located within a cluster (see the lower row of Fig. 1) are determined from the flux enclosed within a polygon fitted around the emission profile of the source; this is determined by the noise level for an extended source manually fitted around the emission for a cluster source, which follows the same strategy used in the construction of the CORNISH survey catalog (Purcell et al. 2013). The observational results of the extended sources or cluster sources in the sample such as flux density (defined as the difference between the aperture summed flux and background flux density divided by the beam-area), angular diameters (defined as intensity-weighted diameter) as well as the uncertainties can be measured by aperture photometry (for details of the aperture photometry method that we used see Sect. 5.3.2 of Purcell et al. 2013).

Analysis of the X-band and K-band maps towards 7 young H II regions (marked by † in Table 1) revealed them to be too confused to obtain reliable results and so these have been excluded. In addition, we add 5 sources identified as UC H II regions in CORNISH by Purcell et al. (2013) that are located within our fields and have rising spectra between C-band and X band in this work. Thus, the final observed sample consists of 112 H II regions. In Table 3, we give the observational results and the derived properties for all of these sources.

In Table 4, we provide a statistical summary of the observed and derived properties for each source at both X- and K-bands. We estimate the uncertainties for the flux density and angular

Table 4. Summary of observational results and the derived physical parameters for 116 young H II regions. In Columns (2-5) we give the minimum, maximum, mean± standard deviation, and median values, respectively, of each parameter.

Parameter	x_{min}	x_{max}	$x_{mean} \pm x_{std}$	x_{med}
observational properties at X-band				
$\log[S_{int}$ (mJy)]	0.58	4.20	2.20±0.76	2.20
$\log[S_{peak}$ (mJy/beam)]	0.40	3.04	1.71±0.66	1.68
Angular size θ''	1.68	21.25	4.54±3.76	2.4
observational properties at K-band				
$\log[S_{int}$ (mJy)]	0.33	3.80	1.99 ± 0.74	2.0
$\log[S_{peak}$ (mJy/beam)]	-0.40	2.88	1.23±0.79	1.68
Angular size θ''	0.6	10.24	2.12 ± 1.95	1.34
Physical properties				
$\log[n_e$(cm^{-3})]	3.14	5.65	4.20 ± 0.05	4.10
$diam$ [pc]	0.004	0.81	0.14 ± 0.01	0.08
$\log[EM$ (pc cm^{-6})]	5.96	9.05	7.28± 0.06	7.09
$\log[N_{Ly}$ (s^{-1})]	45.37	49.82	47.81± 0.09	47.95
ν_t [GHz]	0.56	16.67	3.29 ± 0.31	1.95
Dust absorption fraction f_d	0.14	0.99	0.67 ± 0.03	0.75

size at both frequencies to typically be ∼10% by considering the calibration errors and errors of the measurement method (e.g., Murphy et al. 2010; Sánchez-Monge et al. 2013). In Fig. 2, we show the distributions of the derived parameters. The distributions of integrated flux S_{int} and peak flux density S_{peak} in the left- and middle-panel of Fig. 2 are similar at X-band and K-band, which suggests that the majority of sources are optically thin between these frequencies. The X-band shows a slightly higher peak value of S_{int} and S_{peak} than K-band, some of which may be due to the majority of sources having a turnover frequency below X-band and the fluxes start to decrease afterwards following the power-law of $S_\nu \propto \nu^{-0.1}$ at the optically thin regime of an H II region. Some sources may be due to the larger beam at X-band collecting more flux. The X-band has a larger field of view and is more sensitive to larger angular scales than K-band, which is why a larger proportion of the sources detected at X-band are more extended in the right-panel of Fig. 2.

3.2. Radio properties from the SED models

The physical characteristics of H II regions (e.g., emission measure EM, electron density n_e, Lyman-continuum flux N_{Ly}) can be estimated by the observed angular sizes and flux densities at a given frequency, assuming that the continuum emission comes from a homogeneous optically thin ionised gas (e.g., Urquhart
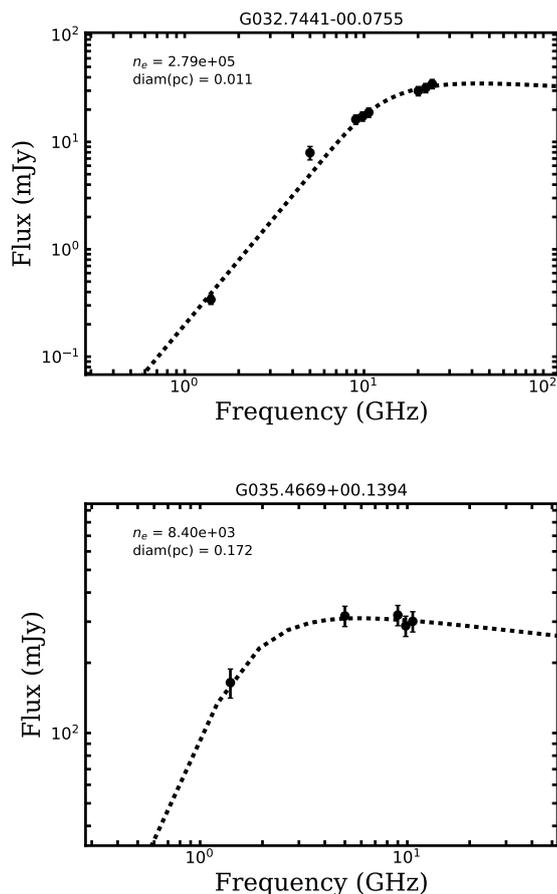
Fig. 3. The upper panel shows the SED fitting to flux density points between 1 and 26 GHz for the compact example G032.7441−00.0755 (upper row of Fig. 1). The lower panel shows the SED fitting to flux density points between 1 and 11 GHz for extended example G035.4669+00.1394 (middle row of Fig. 1) by excluding K-band flux measurements. The best-fitting results for the electron density n_e and physical linear diameter *diam* are shown in the upper left corner of each plot. The best-fitting SEDs for the whole sample are shown in Fig B.1.

et al. 2013; Kalcheva et al. 2018). However, one should keep in mind that the physical properties of young H II regions might be underestimated or overestimated by using a single frequency observation for two reasons: (i) the young H II region might be optically thick at the observed frequency (e.g., Cesaroni et al. 2015); and (ii) the apparent angular size depends on the observing frequency (e.g., Panagia & Felli 1975; Avalos et al. 2006; Yang et al. 2019). Therefore, to determine the properties of young H II regions, it is essential to know their spectral energy distribution (SED) over a wide frequency range that covers both optically thick and thin emission (e.g., Murphy et al. 2010).

We use our multi-wavelength VLA data to construct SEDs for the free-free emission in order to measure the radio properties of our sample of young H II regions. We model each SED for an ionisation-bounded H II region using the standard uniform electron density model given by Mezger & Henderson (1967). In this standard model, the integrated flux density at a given frequency ν is given by $S_\nu = \frac{2k\nu^2 \Omega T_e(1-e^{-\tau})}{c^2}$ using the Rayleigh Jeans approximation, where Ω is the solid angle related to the physical diameter *diam* and distance d of each source. The optical depth τ of free-free radiation can also be represented as a function of frequency (Mezger & Henderson 1967; Dyson & Williams 1997),

$\tau \propto T_e^{-1.35} \nu^{-2.1} n_e^2 \, diam$, where we assume an electron temperature $T_e = 10^4$ K (Dyson & Williams 1997). Therefore, the radio SED of an H II region from the standard model is expected to have a rising spectrum at low frequencies $s_\nu \propto \nu^{+2}$ ($\tau \gg 1$) and a flat spectrum at high frequencies $s_\nu \propto \nu^{-0.1}$ ($\tau \ll 1$). Based on the distances d in Table 1 and the observed fluxes s_ν in Table 2, the SED model of each source has two free parameters, the electron density n_e and the physical diameter *diam*. The best estimate for the two parameters can be obtained by fitting the radio-frequency continuum spectrum of each source. The uncertainty of flux measurements of these points are taken into account in the fitting process. For compact and spherical H II regions in the sample, the derived density n_e and diameter *diam* from SED fitting represent averaged properties over the ionised gas that are responsible for the free-free emission between 1-26 GHz. For the H II regions with non-spherical geometry, this spherical morphology model might introduce additional uncertainty into the determination of the geometry-dependent parameters such as the electron density and diameter. Ideally, the calculation should consider the three-dimensional structure of the volume responsible for the radio emission, however, we don't know the internal structure and any model of the source geometry would introduce additional unknown parameters. In fact, the morphologies of the non-spherical H II regions are variable between X-band and K-band as shown in Fig. B.1. To avoid the complication when calculating the geometry-dependent parameters, the peak physical properties averaged over the beam rather than the entire source are commonly used for these non-spherical and irregular H II regions in previous studies (e.g., Wood & Churchwell 1989; Kurtz et al. 1994). In this work, the uniform spherical model suffices to match the SEDs of the non-spherical H II regions, and the SED of each source has considered the multi-bands radio emission of the entire source. Therefore, the fitted n_e and *diam* represent averaged properties over the entire emission gas at multi-bands and are able to shed light on the physical condition of these non-spherical H II regions as a whole.

In Fig. 3, we show examples of the fitted SEDs for a compact source G032.7441−0.076 and an extended source G035.4669+00.1394. Owing to the lack of short baseline spacings, the K-band flux measurements have been excluded from the SED fitting of the extended sources in the sample. Including the 4 sources with data from archive and references (see Sect. 4 and Table 8), the SEDs and best-fitting models of all 116 H II regions are presented in the Appendix Fig. B.1. The emission measure of each H II region is then calculated using EM = $n_e^2 \times diam$. Considering a mean error of ∼10% both in the flux density at each frequency and the distance measurement, this gives typical errors of ∼20% in n_e, ∼10% in *diam* and ∼40% in EM. The typical errors that we adopted refer to the uncertainty of measurements, as previous studies (e.g., Sánchez-Monge et al. 2013; Kalcheva et al. 2018), and would be larger if considering the uncertainty of the assumptions in the model.

The fitted parameters from radio SEDs are given in Table 5 along with the physical parameters derived from the analysis presented in the following subsection. In the (a), (b), and (c) of Fig. 4, we present the distributions of the fitted parameters. The physical sizes peak at 0.02 pc in the panel (a), and 57% of the sources (66/116) have physical diameters less than 0.1 pc, as shown in the subplot of this panel. This is consistent with the majority of these being classified as UC H II regions or smaller. There are 9 sources with *diam* < 0.01 pc and the mean diameter is *diam* =0.006 pc, corresponding to ∼ 1000 AU. This physical scale implies that the sample could have coincidences with ra-
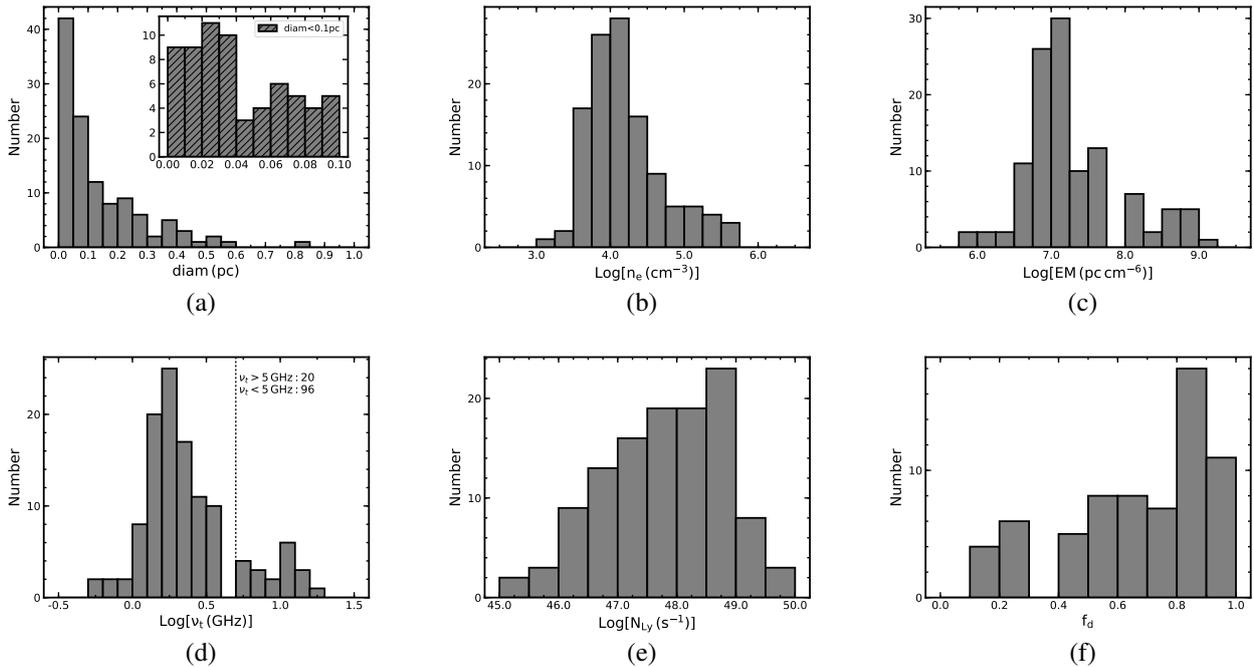
Fig. 4. (a), (b) and (c): distributions of the physical diameter *diam*, the electron density n_e, and the emission measure EM (c) of 116 young H II regions derived from the free-free SED. The bin sizes are 0.05 pc, 0.25 dex, 0.25 dex for *diam*, n_e, and EM, respectively. (d), (e), and (f): distributions of the turnover frequency ν_t (d), the Lyman continuum flux N_{Ly} (e) and the dust absorption fraction f_d (f) of 116 young UC H II regions. The bin sizes are 0.1 dex, 0.1 dex, 0.5 dex for ν_t, f_d, and N_{Ly}, respectively.

dio jets and jet candidates from massive young stellar objects (MYSOs) (Purser et al. 2016).

In Fig. 4 (b), we show the distribution of n_e, which peaks at $10^4 \, cm^{-3}$. About 60% (70/116) of the sources have high densities with $n_e > 10^4 \, cm^{-3}$. The 70 high-density H II regions are compact with a mean diameter of *diam* = 0.06 pc, implying that there might exist small-scale and high-density objects in the sample such as HC H II regions (Kurtz 2005) and MYSO jets (Purser et al. 2016).

In Fig. 4 (c), we show the distribution of emission measure (EM), which peaks at $10^7 \, pc \, cm^{-6}$, and most sources have EM between $3.2 \times 10^6 \, pc \, cm^{-6}$ and $1.0 \times 10^8 \, pc \, cm^{-6}$. There are two groups in the distribution of EM: one with EM $< 10^8 \, pc \, cm^{-6}$ and the other with EM $> 10^8 \, pc \, cm^{-6}$, which indicates that there are sources in the sample connected to the very early stages of H II regions.

The median values of diameter (*diam* =0.08 pc), electron density ($n_e = 1.3 \times 10^4 \, cm^{-3}$) and emission measure (EM= $1.9 \times 10^7 \, pc \, cm^{-6}$) of our sample are consistent with typical values for UC H II regions. About 10% of the sources have $n_e > 10^5 \, cm^{-3}$, 36% of the sample show *diam* < 0.05 pc, and 17% of them have EM $> 10^8 \, pc \, cm^{-6}$, which fulfill the standard quantitative criteria of HC H II regions. We discuss the potential HC H II regions in the sample in Section 4.1.

3.3. Derived physical characteristics

3.3.1. Turnover frequency ν_t

As a dividing line between the optically thin and thick regimes of the radio spectrum of H II region, the turnover frequency ν_t is defined as the frequency where $\tau = 1$ (Kurtz 2005). The flux density of H II region peaks at $\nu > \nu_t$, and decreases as the square of frequency at $\nu < \nu_t$. Using the formula provided in Mezger

& Henderson (1967) for a homogeneous H II region, the optical depth can be expressed as a function of observing frequency ν, electron temperature T_e, which is assumed to be $10^4 \, K$, and emission measure EM:

$$\tau = 0.082 \times \left[\frac{T_e}{K}\right]^{-1.35} \times \left[\frac{\nu}{GHz}\right]^{-2.1} \times \left[\frac{EM}{pc \, cm^{-6}}\right], \quad (1)$$

Setting $\tau = 1$, the turnover frequency can be expressed as (Kurtz 2005):

$$\left[\frac{\nu_t}{GHz}\right] = 0.082 \times \left[\frac{T_e}{K}\right]^{-1.35} \times \left[\frac{n_e^2 \times diam}{cm^{-3} \, pc}\right]^{0.476} \quad (2)$$

The typical error for the ν_t is 30% by considering the typical 20% error in density estimation and 10% in diam measurements. In the panel (d) of Fig. 4, we present the distribution of the turnover frequency ν_t for this young H II regions sample (i.e. young UC H II region sample), which peaks at $\nu_t \sim 2 \, GHz$ and has a mean value of $\nu_t \sim 3.3 \, GHz$. Both of the peak and mean turnover frequencies of this young H II regions sample are lower than the expected value $\sim 5 \, GHz$ of UC H II regions in Kurtz (2005) with typical $n_e \sim 3 \times 10^4 \, cm^{-3}$ and *diam* $\sim 0.1 \, pc$. A lower turnover frequency in the radio spectrum is suggested by models with a non-uniform density profile in Steggles (2016) and Steggles et al. (2017), if a large fraction of detected emission from the optically-thin low-density region surrounded by a H II region. This lower turnover frequency found in the sample may hence indicate that there exists a significant fraction of low-density gas in the surroundings of H II regions in the sample. Alternatively, many of these H II regions are simply optically thin.

The Fig. 4 (d) indicates two populations of H II regions: one with $\nu_t < 5 \, GHz$ and the other with $\nu_t > 5 \, GHz$, which are referred to as optically-thin and optically-thick H II regions in this

work, respectively. The optically-thick H II regions are found to have higher density, higher emission measure, and smaller physical linear size compared to optically-thin H II regions, as shown in Table 6.

3.3.2. Lyman continuum flux

For an optically-thin H II region in the photoionization equilibrium, the Lyman continuum ionising flux N_{Ly} emitted by the embedded massive star can be calculated from the radio continuum flux and heliocentric distance to the source (Sánchez-Monge et al. 2013), as

$$\left[\frac{N_{Ly}}{s^{-1}}\right] = 8.9 \times 10^{40} \left[\frac{S_\nu}{Jy}\right]\left[\frac{\nu}{GHz}\right]^{0.1}\left[\frac{T_e}{10^4 K}\right]^{-0.45}\left[\frac{d}{pc}\right]^2, \quad (3)$$

where S_ν is the integrated flux density at frequency ν, T_e is electron temperature assumed to be 10^4 K and d is the distance to the source. For each source in the sample, we use the S_ν measured in the optically-thin part of the radio SED to calculate the Lyman continuum flux. The distance for each source is taken from the literature (as discussed in Sect. 2.1). The typical error of the derived Lyman continuum flux is $\sim 40\%$ considering the error in both kinematic distance and the integrated flux measurement (e.g., Urquhart et al. 2013).

The distribution of the derived Lyman continuum flux is shown in Fig. 4 (e), which peaks at 10^{48} s^{-1} and ranges from $10^{45.4}$ s^{-1} to $10^{49.9}$ s^{-1}. The corresponding spectral type of the zero-age main-sequence (ZAMS) stars are between B0 to O4 listed in Table 5, by assuming that a single star is responsible for the ionization and there is no dust in the ionization-bounded H II region (e.g., Garay et al. 1993; Wood & Churchwell 1989). The derived spectral type of the ZAMS star would be earlier or later (e.g., Wood & Churchwell 1989), if multiple stars are responsible for the ionization or if there is dust absorption within the H II region (e.g., Garay et al. 1993). For instance, the presence of dust may lower the flux a factor of 2 or more as the dust absorption fraction ranges from $\sim 50\%$ to $\sim 90\%$ for UC H II regions (e.g., Wood & Churchwell 1989; Garay et al. 1993; Kurtz et al. 1994), but if the emission was from a cluster then the spectral type would be typically earlier by a subclass or two (Wood & Churchwell 1989; Urquhart et al. 2013). The effects of cluster and dust on determining the spectral type are probably comparable and counterbalanced each other. So the values we estimated are reliable within a few sub-classes.

3.3.3. Dust within H II regions

Previous studies found that a significant fraction of the Lyman continuum photons is absorbed by the dust within H II regions (Garay et al. 1993; Wood & Churchwell 1989; Kim & Koo 2001). By assuming that a single star is responsible for the observed luminosity and the observed Lyman continuum flux of an H II region, the fraction of UV photons absorbed by dust within H II regions is defined as (e.g., Wood & Churchwell 1989): $f_d = 1 - N'_c/N^\star_c$, where N'_c is the number of observed ionizing photons and $N^\star_c$ the predicted Lyman continuum photons derived from spectral type based on the total infrared luminosity. As discussed in the previous studies (e.g., Garay et al. 1993; Wood & Churchwell 1989), f_d should be taken as an upper limit as it is very likely to be overestimated if the expected Lyman continuum photons are excited by clusters of young stars rather than by a single star. For instance, at a given total luminosity, the

spectral type estimated assuming a cluster that provides the entire infrared luminosity is typically two or three subclasses later than the spectral type estimated assuming a single star (Wood & Churchwell 1989), and thus leads to a lower expected Lyman continuum flux $N^\star_c$ than derived assuming a single star. The observed N'_c would be dominated by the earliest spectral type in the clusters as the properties of O-type stars change so dramatically between two subclasses (e.g., Panagia 1973; Wood & Churchwell 1989), which has also been found by Urquhart et al. (2013) who suggested that the most massive stars within clumps dominate the observed properties. The upper limit of the fraction of Lyman continuum photons absorbed by dust within H II regions can range from 50% (Garay et al. 1993; Kim & Koo 2001) to 90% (Wood & Churchwell 1989; Kurtz et al. 1994).

There is evidence of dust existing in the H II regions in our sample since all of them show bright $24\mu m$ emission in the MIPSGAL survey (Carey et al. 2009) and strong $70\mu m$ emission in the Hi-GAL survey (Molinari et al. 2010), at a high angular-resolution ($\sim6''$). After excluding $\sim40\%$ of the sources with Lyman excess (see Sect. 5.2), the upper limit of the mean fraction absorbed by dust within H II regions for our sample is $f_d = 0.67 \pm 0.03$, which is consistent with previous results (e.g., Garay et al. 1993; Kim & Koo 2001; Wood & Churchwell 1989), as shown in the panel (f) of Fig. 4. Among the 67 H II regions with dust absorption, 43% (29/67) of the sources with physical diameters $diam < 0.1$ pc have a mean of $f_d = 0.79 \pm 0.04$, and 57% (38/67) of the sources with $diam > 0.1$ pc have a mean of $f_d = 0.58 \pm 0.04$. This indicates that the dust absorption fraction tends to be more significant for the more compact, and presumably younger H II regions compared to the larger and more evolved H II regions, which agree with the model in Arthur et al. (2004) that the fraction of ionizing photons in H II regions absorbed by dust decreases with time.

4. Classification and properties of the optically thick sources

4.1. Classification of the optically-thick H II regions

In Sect. 3.3.1 we identified 20 young optically-thick H II regions with turnover frequencies larger than 5 GHz. Since the turnover frequency of an UC H II region is ~5 GHz (Kurtz 2005), the 20 optically-thick H II regions are very likely to be in the HC H II region stage or in an intermediate stage connecting the HC H II region and UC H II region stages. The quantitative criteria for HC H II regions, UC H II regions and the intermediate objects between the two stages, are presented in Table 7, which are summarised from the literature (e.g., Wood & Churchwell 1989; Kurtz et al. 1994; Afflerbach et al. 1996; Kurtz 2005; Hoare et al. 2007) .

Among the 20 optically-thick H II regions, 7 sources are associated with previously identified HC H II regions that have been summarised in Table 1 of Yang et al. (2019). In Fig. 5 we show the distribution of the electron densities, emission measures and physical diameters of these regions. On this plot we indicate the region of parameter space where HC H II regions are expected to reside (i.e. $n_e > 10^5$ cm^{-3} and $diam < 0.05$ pc). Fourteen of the optically thick H II regions satisfy these criteria. The remaining sources all satisfy the size criterion for HC H II regions but their electron densities are too low and so these are considered to be intermediate between the HC H II and UC H II regions stages.

In Figure 6-8, we present three-colour infrared maps of each H II region. In these maps, we include contours of the dust and radio emission and any coincident masers, so we can investigate

Table 5. Derived physical properties of 116 young H II regions.

Name	n_e (10^5 cm^{-3})	$diam$ (pc)	EM (10^7 pc cm^{-6})	ν_t (GHz)	$\log N_{Ly}$ (photons s^{-1})	Spectral Type	f_d
(1)	(2)	(3)	(4)	(5)	(6)	(7)	(8)
G010.3009−00.1477	0.09	0.119	0.92	1.69	47.94	O9.5	0.86
G010.4724+00.0275	1.43	0.022	45.2	10.77	48.11	O9	0.94
G010.6234−00.3837	0.16	0.166	4.39	3.55	48.9	O6.5	0.81
G010.9584+00.0221	0.36	0.029	3.78	3.31	47.35	B0	-
G011.0328+00.0274	0.13	0.014	0.24	0.89	45.57	B1	-
G011.1104−00.3985	0.07	0.145	0.62	1.4	47.94	O9.5	0.27
G011.1712−00.0662	0.09	0.053	0.45	1.21	46.91	B0	-
G011.9368−00.6158	0.07	0.155	0.86	1.63	48.12	O9	0.19
G011.9446−00.0369	0.17	0.075	2.2	2.56	47.84	O9.5	-
G012.1988−00.0345	0.07	0.148	0.65	1.43	47.98	O9	0.77

Notes. Only a small portion of the data is provided here, the full table is presented in Table A.3 and will be available in electronic form at the CDS.

Table 6. Summary of the derived physical parameters for the 96 optically-thin H II regions ($\nu_t < 5$ GHz) and the 20 optically-thick H II regions ($\nu_t > 5$ GHz). In Columns (2-5), we give the minimum, maximum, mean± standard deviation, and median values, respectively, of each parameter.

| Parameter	x_{min}	x_{max}	$x_{mean} \pm x_{std}$	x_{med}
The 20 optically-thick H II regions sample				
$\log[n_e (\mathrm{cm}^{-3})]$	4.37	5.65	5.11± 0.07	5.12
$diam$ [pc]	0.004	0.23	0.035 ± 0.01	0.023
$\log[\mathrm{EM} (\mathrm{pc\,cm}^{-6})]$	8.00	9.05	8.50± 0.08	8.58
$\log[N_{Ly} (\mathrm{s}^{-1})]$	46.21	49.55	47.77± 0.20	47.80
ν_t [GHz]	5.28	16.67	9.73 ± 0.80	9.94
Dust absorption fraction f_d	0.16	0.99	0.81 ± 0.05	0.88
The 96 optically-thin H II regions sample				
$\log[n_e (\mathrm{cm}^{-3})]$	3.15	4.69	4.02± 0.03	4.01
$diam$ [pc]	0.006	0.81	0.16 ± 0.02	0.11
$\log[\mathrm{EM} (\mathrm{pc\,cm}^{-6})]$	5.96	7.73	7.16 ± 0.04	7.02
$\log[N_{Ly} (\mathrm{s}^{-1})]$	45.37	49.83	47.82± 0.1	47.97
ν_t [GHz]	0.56	3.60	1.91 ± 0.08	1.80
Dust absorption fraction f_d	0.14	0.97	0.62 ± 0.03	0.66

Table 7. Quantitative criteria for HC H II regions, UC H II regions and intermediate objects (HC H II → UC H II) between the two stages, summarized from the literature.

Parameters	HC H II	HC H II → UC H II	UC H II
Size (pc)	$\lesssim 0.05$	$\sim [0.05 - 0.1]$	$\lesssim 0.1$
n_e (cm^{-6})	$\gtrsim 10^5$	$\sim [10^4 - 10^5]$	$\gtrsim 10^4$
EM (pc cm^{-6})	$\gtrsim 10^8$	$\sim [10^7 - 10^8]$	$\gtrsim 10^7$
RRL ΔV (km s^{-1})	$\gtrsim 40$	$\sim [25 - 40]$	< 40

their environments and associations with other star formation tracers. We individually discuss the properties of the optically thick H II regions with respect to their environment, their association with dense gas, and star formation tracers in the following subsections, and we follow the order that is presented in Table 8.

4.1.1. HC H II regions and candidate HC H II regions identified in this work

G010.4724+00.0275: This source is located in the G10.47+0.03 complex region that hosts three UC H II re-
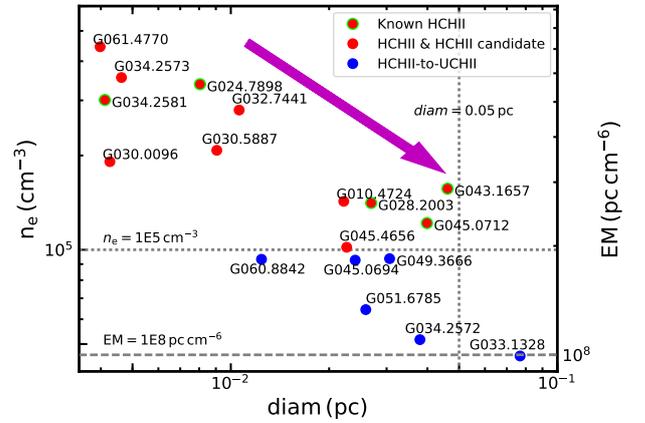
Fig. 5. Distribution of properties of 20 optically-thick HC H II regions identified in Sect. 3.3.1; we have excluded 2 objects (G043.1652 & G043.1665) in the optically-thick sample that are associated with un-recovered HC H II region marked by ∗ listed in Table 8 (see Sect. 4.1.3). The red filled circles with lime circles identify the previously known HC H II regions while the red filled circles are associated with the 6 HC H II regions and HC H II region candidates identified in this work. The filled blue circles identify the 5 H II regions that are intermediate between the HC H II and UC H II region stages. The vertical and horizontal dotted and dashed lines indicate the standard quantitative criteria of an HC H II region. There is a clear evolutionary trend from HC H II region to the stage between HC H II region and UC H II region in the physical parameter space, as indicated by a magenta arrow.

gions (Wood & Churchwell 1989), water masers (Hofner & Churchwell 1996), 6.7 GHz methanol masers (Pestalozzi et al. 2005), various complex molecules (Hatchell et al. 1998), and massive molecular outflows along the NE-SW direction (López-Sepulcre et al. 2009). This object is resolved into two compact sources, G10.47+0.03A and G10.47+0.03B, in Wood & Churchwell (1989) with a resolution of 0.4″, which is also seen in the K-band emission shown as contours in the upper-left panel of Fig. 7 with two blended compact components. The radio source is positionally coincident with methanol and water masers, a bright mid-infrared point source and is embedded in a dense molecular clump as traced by the ATLASGAL emission, and therefore clearly associated with star formation activity. Its physical properties such as $n_e = 1.43 \times 10^5$ cm^{-3}, $diam = 0.022$ pc, EM = 4.52×10^8 pc cm^{-6}, and $\log N_{Ly} = 48.11$,

Table 8. Summary of the physical parameters and the classification of the 20 optical thick H II regions identified in this work. The classifications given in col. 6 are HC H II regions (Class: HC), HC H II region candidates (Class: HC?), and intermediate objects (Class: HC-UC); these have been assigned based on their electron density n_e, physical diameter *diam* and emission measure EM, derived from the SED fitting method. We also include four sources with $\nu_t \sim 3.5$ GHz , such as G010.9584+00.0221 and G035.5781−00.0305 that have previously been identified as HC H II regions but not recovered by this work (see Sect. 4.1.3), as well as G030.8662+00.1143 and G030.7197-00.0829 that show broad RRL with $\Delta V > 40$ km s^{-1}.

| Name	n_e	*diam*	EM	ΔV(RRL)[ref.]	Class	log[L_{bol}]	log[N_{Ly}]	Maser	clump
	(10^5 cm^{-3})	(pc)	(10^8 pc cm^{-6})	(km s^{-1})		($L_\odot$)	(s^{-1})	emission?	outflow?
(1)	(2)	(3)	(4)	(5)	(6)	(7)	(8)	(9)	(10)
HC H II and candidate HC H II identified in this work									
G010.4724+00.0275	1.43	0.022	4.52	-	HC?	5.7	48.11	Yes	Yes
G024.7898+00.0833†	3.38	0.008	9.18	40 (H66α)[1]	HC	5.2	47.52	Yes	Yes
G028.2003-00.0494†	1.41	0.027	5.35	74(H92α)[2]	HC	5.1	48.37	Yes	Yes
G030.0096-00.2734	1.91	0.0043	1.56	-	HC?	3.8	46.21	Yes	Yes
G032.7441-00.0755	2.79	0.011	8.28	40.3(Hnα)[3]	HC	5.0	47.69	Yes	Yes
G034.2573+00.1523	3.55	0.0046	5.82	48.7(H42α)[3]	HC	4.8	46.58	Yes	Yes
G034.2581+00.1533†	3.01	0.0041	3.73	48.4(H76α)[2]	HC	4.8	46.54	Yes	Yes
G043.1657+00.0116†	1.57	0.046	11.32	63.9(H66α)[4]	HC	6.9	48.69	Yes	Yes
G045.0712+00.1321†	1.22	0.040	5.89	40(H76α)[5]	HC	5.7	48.73	Yes	Yes
G045.4656+00.0452	1.02	0.023	2.36	47.8(H39α)[3]	HC	5.0	47.88	Yes	Yes
G061.4770+00.0892	4.45	0.0040	7.88	-	HC?	5.1	46.81	Yes	Yes
G030.5887−00.0428★	2.08	0.009	3.91	56.2(H40α)[3]	HC	4.0	47.28	Yes	Yes
Intermediate objects (HC H II → UC H II regions)									
G034.2572+00.1535	0.52	0.038	1.01	22.8(H76α)[2]	HC−UC	4.8	48.03	Yes	Yes
G045.0694+00.1323	0.74	0.026	1.40	16.7(H92α)[2]	HC−UC	5.7	47.76	-	Yes
G049.3666−00.3010	0.94	0.031	2.69	34.5(H40α)[3]	HC−UC	5.1	48.05	Yes	Yes
G051.6785+00.7193	0.64	0.026	1.07	-	HC−UC	5.0	47.68	Yes	Yes
G060.8842−00.1286	0.93	0.012	1.08	-	HC−UC	4.2	46.40	Yes	Yes
G030.7197−00.0829★	0.22	0.093	0.45	43.0(H40α)[3]	HC−UC	4.7	48.44	Yes	Yes
G030.8662+00.1143★	0.37	0.031	0.43	44.9(H39α)[3]	HC−UC	4.1	47.46	Yes	Yes
G033.1328−00.0923★	0.21	0.10	0.46	43.0(H39α)[3]	HC−UC	5.0	48.54	Yes	Yes
Previously identified HC H II regions not resolved in the current work									
G010.9584+00.0221∗	0.36	0.029	0.38	43.8(H92α)[2]	HC	4.0	47.35	Yes	Yes
G035.5781−00.0305∗	0.22	0.093	0.45	50.0(H42α)[3]	HC	5.3	48.36	Yes	Yes
G043.1652+00.0129∗	0.88	0.053	4.15	53.7(H66α)[2]	HC	6.9	48.91	Yes	Yes
G043.1665+00.0106∗	0.24	0.22	1.22	48.6(H66α)[2]	HC	6.9	49.55	Yes	Yes

References: 1. Beltrán et al. (2007); 2, Sewilo et al. (2004); Sewiło et al. (2011); 3, Kim et al. (2017); 4, De Pree et al. (1997); 5, Keto et al. (2008); 6, (Zhang et al. 2014). Notes: for G032.7441−00.0755, the RRL Hnα indicates n=39,40,41,42. Symbols † and ∗ indicate the known HC H II regions summarised in Table 1 of Yang et al. (2019). Symbol ★ represents the four H II regions with data from literature and archive.

imply that it is likely to be an HC H II region. Its natal clump has a mass of $2.57 \times 10^4\ M_\odot$ and a bolometric luminosity of 5.0 $\times 10^5\ L_\odot$ (Urquhart et al. 2018). Its spectral type O5.5 derived from the bolometric luminosity is earlier than O9 derived from Lyman continuum flux, which supports the hypothesis that this source is located in a cluster, as reported in Pascucci et al. (2004).

G024.7898+0.0833: This source is an HC H II region identified by Beltrán et al. (2007), which is found to be associated with many CH_3OH masers (Surcis et al. 2015; Bartkiewicz et al. 2016) and OH masers (Forster & Caswell 2000; Caswell et al. 2013), H_2O masers (Caswell et al. 1983; Forster & Caswell 2000), and outflows traced by CO (Furuya et al. 2002; Beltrán et al. 2011) and SiO (Codella et al. 2013). Its physical properties such as n_e, *diam*, and EM (Table 8) are consistent with previous results (Beltrán et al. 2007; Cesaroni et al. 2019). Its natal clump has a mass of $7.64 \times 10^3\ M_\odot$ and a bolometric luminosity of $1.58 \times 10^5\ L_\odot$ (Urquhart et al. 2018). The spectral type of this HC H II region O6.5 derived from the infrared luminosity is

much earlier than O9.5 derived from the Lyman continuum flux (Table 1) that includes contributions from the nearby UC H II region G024.7889+00.0824 in the field. The possible explanation for the discrepancy of spectral type is that this source is located in a cluster or/and a significant amount of Lyman continuum photons are absorbed by the surrounding dust, with an upper limit of dust absorption fraction $f_d = 92\%$ (see Sects. 3.3.2 and 3.3.3). Since this HC H II region shows extended 4.5 μm emission, it is associated with an extended green object as defined by Cyganowski et al. (2008).

G028.2003−0.0494: This source is a known HC H II region identified by Sewilo et al. (2004), which is found to be associated with the 37.7 GHz CH_3OH maser (Ellingsen et al. 2011), OH masers (Argon et al. 2000; Caswell et al. 2013), and H_2O masers (Urquhart et al. 2011). Its physical properties such as n_e, *diam*, and EM listed in Table 8 are consistent with previous results (Sewiło et al. 2011). Its natal clump has a mass of $4.45 \times 10^3\ M_\odot$ and a bolometric luminosity of $1.30 \times 10^5\ L_\odot$ (Urquhart et al. 2018), which is associated with molecular out-
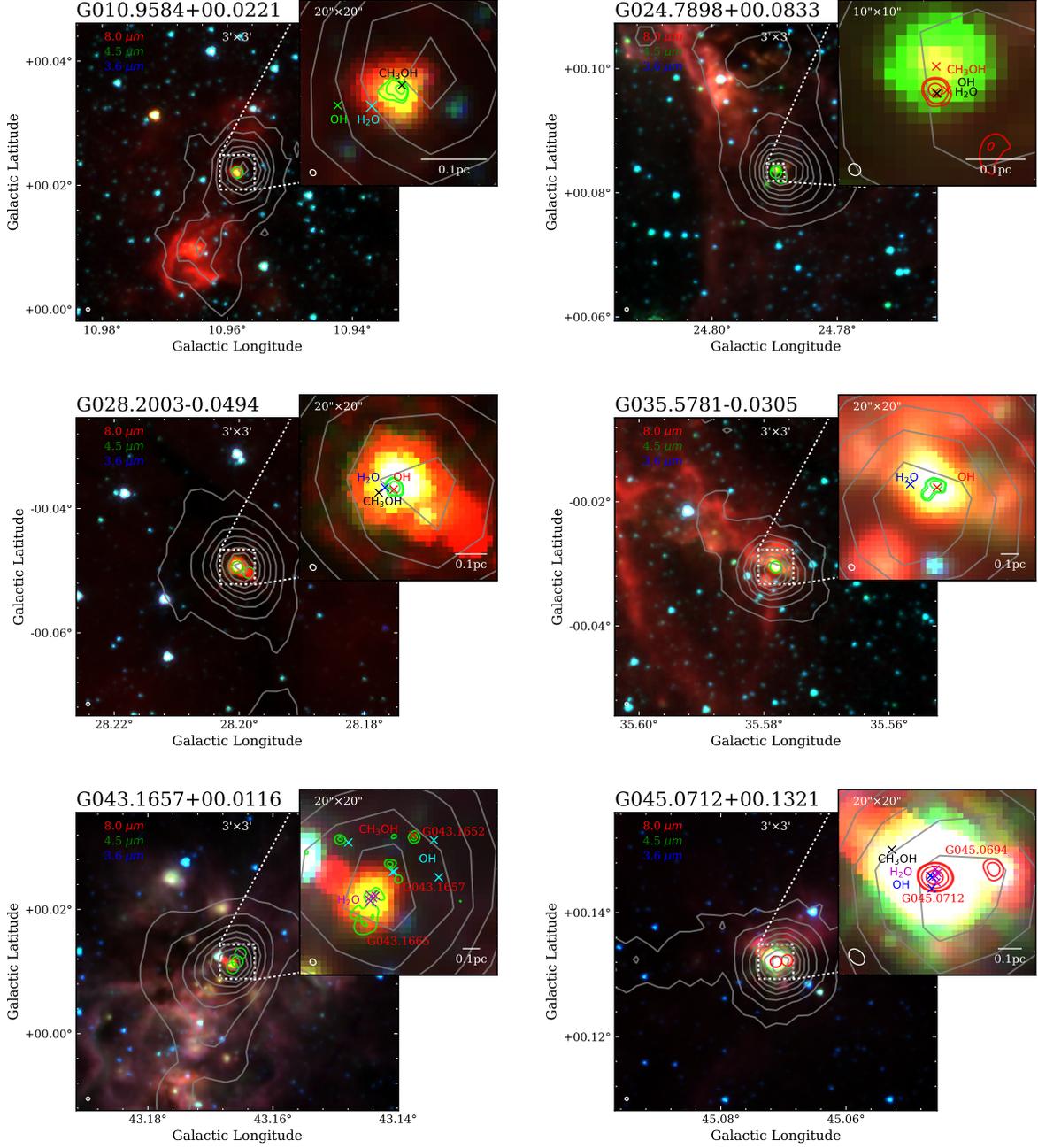
Fig. 6. Three-color composition image (or RGB image) from *Spitzer* GLIMPSE 8 μm (red), 4.5 μm (green), 3.6 μm (blue) bands (Benjamin et al. 2003; Churchwell et al. 2009) for the 8 HC H II regions discussed in Sect. 4. Lime or red circles show the radio sources in the field from the CORNISH survey. The upper-right of the zoom-in images show the peak position of H_2O maser (magenta cross) and OH maser (black cross), and the linear scalebar of 0.1 pc in white. Grey contours in the image show 870 μm emission from ATLASGAL (Schuller et al. 2009), and the lime (or red) contours show K-band 22 GHz emission presented in this work. The red contours in the bottom-right show X-band 10 GHz emission as the K-band emission is missing for source G045.0694. The FWHM beam of GLIMPSE (2″) and K-band observations are indicated by the white circles shown in the lower-left corner of each image.

flows (Maud et al. 2015; Yang et al. 2018). Its spectral type O6.5 derived from the bolometric luminosity is earlier than O7.5 derived from the Lyman continuum flux that includes the contribution from its nearby UC H II region G028.1985−00.0503 with $N_{\rm Ly} = 5.0 \times 10^{47}$. This could be the result of this source being located in a cluster, as shown in the middle-left panel of Fig. 6, or be due to the finding that about 43% of the Lyman continuum photons are absorbed by the surrounding dust.

G030.0096−00.2734: This compact radio source, located in the W43 star-forming complex (e.g., Blum et al. 1999; Medina et al. 2019; Gao et al. 2019), is the first one in the sample that is associated with an infrared dark cloud (G030.01−0.27; Battersby et al. 2011), which itself is associated with many molecular lines (Schlingman et al. 2011) as well as methanol masers (Breen et al. 2015). Its natal clump AGAL030.008−0.272 is associated with a molecular outflow identified by Yang et al. (2018), which has a maximum outflow velocity of 4.5 km s^{-1}. It
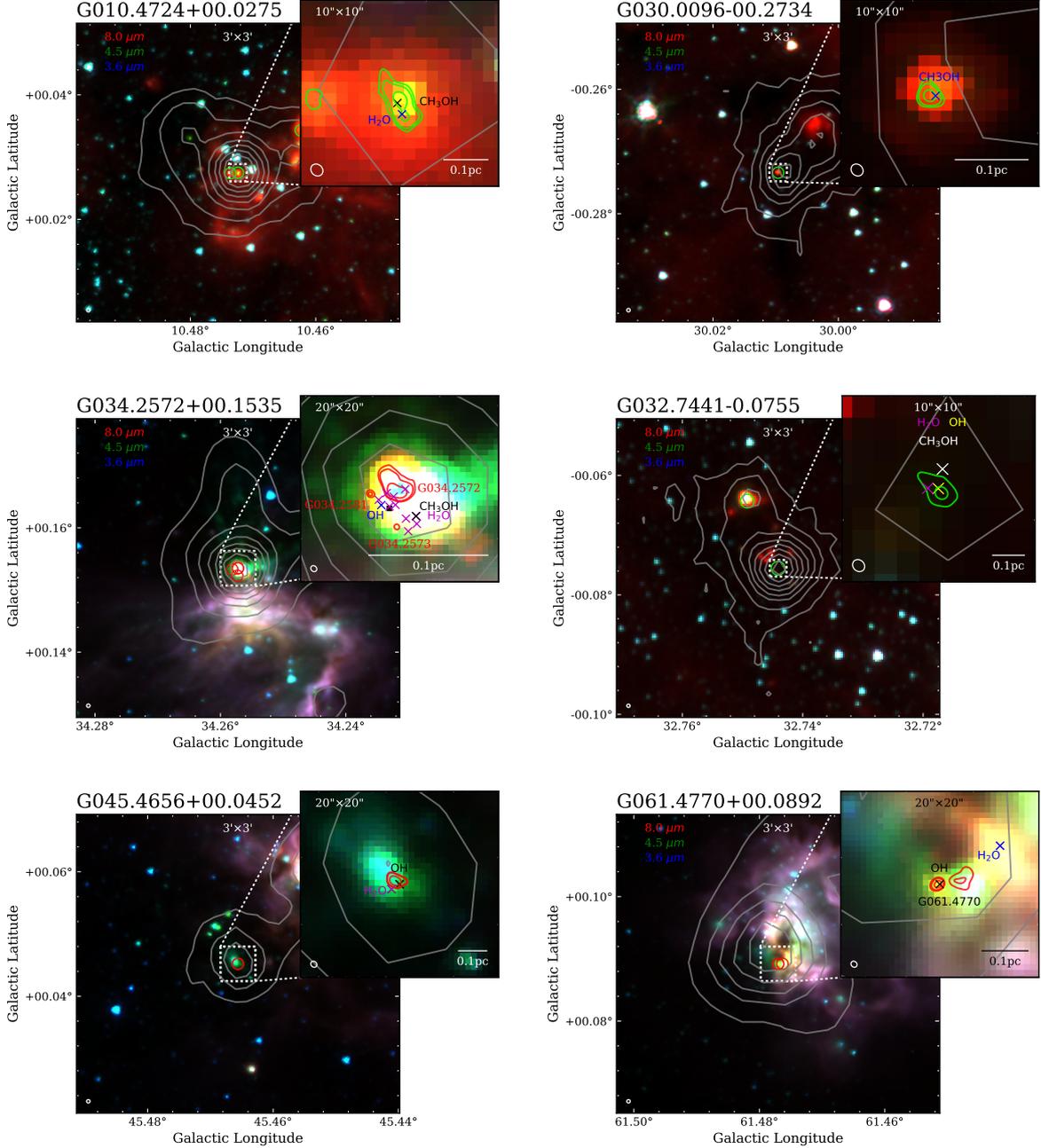
Fig. 7. As described in Fig. 6, except in this case the sources include newly identified HC H II regions and intermediate objects. The grey contours in the image of G061.4770+00.0892 show the 500μm emission from Hi−GAL.

is the only radio source in its natal clump, and its spectral type B1 derived from the bolometric luminosity is consistent with B0.5 derived from the Lyman continuum photons, indicating a lack of dust within this H II region. The radio emission is coincident with a compact mid-infrared point source confirming it is associated with an embedded protostellar object. The physical properties of G030.0096−00.2734 are consistent with this source being an HC H II region at a very early evolutionary stage.

G030.5887−00.0428: This source shows compact radio emission at 5 GHz CORNISH, as shown in the middle-right of Fig. 8. Its flux densities at high frequencies were obtained in project VLA18A-066, with 217.70 mJy at 15.5 GHz, and 223.53 mJy at

16.5 GHz. With flux densities at low frequency of 1.4 GHz and 5 GHz (summarised in Yang et al. 2019), its physical properties can be determined from the radio SED. Water, hydroxyl, and methanol masers sites (Argon et al. 2000; Pestalozzi et al. 2005; Urquhart et al. 2011) are detected in its vicinity and molecular outflows (Yang et al. 2018) are found to be associated with its natal clump. Its natal clump AGAL030.588−00.042 has a mass of 758 $M_\odot$ and a bolometric luminosity of $1.12 \times 10^4\,L_\odot$ (Urquhart et al. 2018), and shows a broad millimeter RRL H40α with $\Delta V = 56.2\,\mathrm{km\,s}^{-1}$ (Kim et al. 2017). It is the only radio source in the parent clump, and its spectral type B0.5, obtained from the bolometric luminosity, is consistent with that of a B0 star derived from the radio luminosity, indicating the absence of dust within this H II region. The broad RRL line, compact size

and high electron density are consistent with this source being classified as an HC H ɪɪ region.

G032.7441−00.0755: The radio emission associated with this source is weak and very compact and there is bright emission at $70\mu m$ from the Hi−GAL survey (Molinari et al. 2010), while no counterpart is seen at mid-infrared wavelengths ($8\mu m$; see the middle-right panel of Fig. 7). This source was found to host H_2O masers (Caswell et al. 1983), OH masers (Caswell et al. 2013) and CH_3OH masers (Bartkiewicz et al. 2016), and is associated with CO outflows (Yang et al. 2018), broad molecular lines such as SiO (2-1) (Csengeri et al. 2016), N_2H^+, and HCO^+ (Shirley et al. 2013) and millimeter RRLs ($\Delta V = 40.34\,km\,s^{-1}$; Kim et al. 2017). The blue-shifted and red-shifted methanol masers spots mapped by Bartkiewicz et al. (2016) have a similar orientation as the blue-shifted and red-shifted outflows mapped by Yang et al. (2018). Its physical parameters ($n_e = 2.79 \times 10^5\,cm^{-3}$, $diam = 0.011\,pc$, EM $= 8.28 \times 10^8\,pc\,cm^{-6}$, $\nu_t = 14.37\,GHz$) are consistent with other HC H ɪɪ regions and we therefore identify this as a new mid-infrared dark HC H ɪɪ region detection. Fig. 7 shows that it is the only radio source in its natal clump. Its spectral type O7 derived from the bolometric luminosity is earlier than O9.5 derived from the Lyman continuum flux, indicating about 88% of the Lyman continuum photons were absorbed by dust within this H ɪɪ region. It could be the best example to trace the dynamics associated with the final stages of accretion in massive star formation since it is still dark at $8\mu m$ and covers a significant broad component of ionised gas (e.g., RRL), shocked gas (e.g., SiO) and molecular gas (e.g., CO).

G034.2572, G034.2573 and G034.2581: These three H ɪɪ regions lie in G34.26+0.15, a well-studied complex region that contains three UC H ɪɪ regions (Wood & Churchwell 1989; Sewilo et al. 2004): G34.26+0.15A (G034.2573+00.1523), G34.26+0.15B (G034.2581+00.1533) and G34.26+0.15C (G034.2572+00.1535); these are marked with red circles in the middle-left panel of Fig. 7. This complex also hosts H_2O masers (Hofner & Churchwell 1996), OH masers (Forster & Caswell 1999; Ruiz-Velasco et al. 2016), CH_3OH masers (Breen et al. 2015) and numerous molecules (Fu & Lin 2016; Kim et al. 2000), as well as infall/outflows traced by CO or water masers (e.g. Wyrowski et al. 2016; van der Tak et al. 2019; Yang et al. 2018; Imai et al. 2011). Broad radio recombination lines (RRLs) are detected in G34.26+0.15B and G34.26+0.15C with a line-width of $\Delta V > 40\,km\,s^{-1}$ (Sewilo et al. 2004). This is also found in their natal clump AGAL034.258+00.154 (Kim et al. 2017, 2018). G34.26+0.15B is considered to be a HC H ɪɪ region candidate (G034.2581+00.1533, Sewilo et al. 2004; Yang et al. 2019), which is blended with G34.26+0.15C in the C-band and X-band images, and is only resolved in higher resolution K-band image. G034.2572+00.1535 is associated with G34.26+0.15C, which is an extended source, and can be resolved into three compact sources, all of which have RRL line widths $\Delta V > 40\,km\,s^{-1}$ (Sewilo et al. 2004).

G034.2572+00.1535 is very likely to host candidates in an evolutionary stage between HC H ɪɪ region and UC H ɪɪ region. The nearby source G034.2573+00.1523 is also likely to be associated with an HC H ɪɪ region.

G043.1652, G043.1657 and G043.1665: These three sources are located in the well-known star-forming region W49A complex that is associated with CO outflows (Scoville et al. 1986).

As shown in the bottom-left panel of Fig. 6, the three sources are associated with three HC H ɪɪ regions such as W49A A (G043.1652+00.0129), W49A B (G043.1657+00.0116), and W49A G (G043.1665+00.0106) in the W49A complex (De Pree et al. 1997, 2004; Sewilo et al. 2004), which are found to be associated with many CH_3OH (Bartkiewicz et al. 2014; Breen et al. 2015), OH (Argon et al. 2000), and H_2O (De Pree et al. 2000; Urquhart et al. 2011) masers. G043.1657+00.0116 (W49A B) has $n_e = 1.57 \times 10^5\,cm^{-3}$, $diam = 0.046\,pc$, EM $= 11.32 \times 10^8\,pc\,cm^{-6}$, and $\log N_{Ly} = 48.69$, which is consistent with the typical value of HC H ɪɪ regions, as reported by De Pree et al. (2000).

G043.1652+00.0129 (W49A A) is resolved into two compact components at higher resolution $\sim 0.05''$ (De Pree et al. 2000, 2004). Its physical properties such as $n_e = 0.88 \times 10^5\,cm^{-3}$, $diam = 0.053\,pc$, EM $= 4.15 \times 10^8\,pc\,cm^{-6}$, and $\log N_{Ly} = 48.91$, are consistent with previous results in De Pree et al. (1997) for W49 A at a similar resolution of $\sim 1''$. However, the derived properties are slightly below the typical values of HC H ɪɪ regions and also show smaller n_e, smaller EM and larger $diam$ compared to the results measured at higher resolution ($0.05''$) with $n_e = 6.1 \times 10^5\,cm^{-3}$, $diam = 0.056\,pc$, EM $= 83 \times 10^8\,pc\,cm^{-6}$ (De Pree et al. 2000). This might be due to our observation including not only the two compact components but also a larger fraction of optically-thin emission around them.

G043.1665+00.0106 (W49A G) is also multiply peaked at higher resolution $\sim 0.05''$ (De Pree et al. 2000, 2004). Its physical properties such as $n_e = 0.24 \times 10^5\,cm^{-3}$, $diam = 0.24\,pc$, EM $= 1.22 \times 10^8\,pc\,cm^{-6}$, and $\log N_{Ly} = 49.55$, are consistent with the results in de Pree et al. (1996) for W49A G. The n_e is slightly smaller compared to the measurements at higher resolution with $n_e > 1.0 \times 10^5\,cm^{-3}$ for the two main compact components (De Pree et al. 2000), which may result from the large amount of optically-thin emission around these compact components.

G045.0712 and G045.0694: The radio emission consists of two distinct sources: the stronger source G045.0712+00.1321 and the weaker source G045.0694+00.1323, offset by $\sim6''$ (as shown in the bottom-right panel of Fig. 6). G045.0712+00.1321 has previously been identified as an HC H ɪɪ region by Keto et al. (2008) and Sewiło et al. (2011) (G45.07+0.13 NE). The physical properties of G045.0712+00.1321 indicate that this HC H ɪɪ regions is associated with a O6.5 type massive star, which supports the previous results and classification by Sewiło et al. (2011). The fainter of the two, G045.0694+00.1323, is likely to be transitioning into an UC H ɪɪ region, based on the distribution of radio properties shown in Fig. 5. Their radio emission is coincident with a bright extended infrared source and a dense submillimeter clump AGAL045.071+00.132 in Urquhart et al. (2018). The natal clump is associated with extended molecular outflows with W-E direction (Yang et al. 2018). This source is also host to H_2O masers (Hofner & Churchwell 1996), OH masers (Argon et al. 2000), and CH_3OH masers (Kurtz et al. 2004). The presence of two very young H ɪɪ regions, molecular outflows, and three different species of masers would suggest that this clump hosts a young proto-cluster.

G045.4656+00.0452: This compact radio source is embedded in a dense molecular clump and is associated with an extended mid-infrared source, as well as water (Forster & Caswell 1999) and OH (Argon et al. 2000) maser emissions (see bottom-left panel of Fig. 7). Its natal clump AGAL045.466+00.046 is also associated with bipolar outflows (Yang et al. 2018) and broad
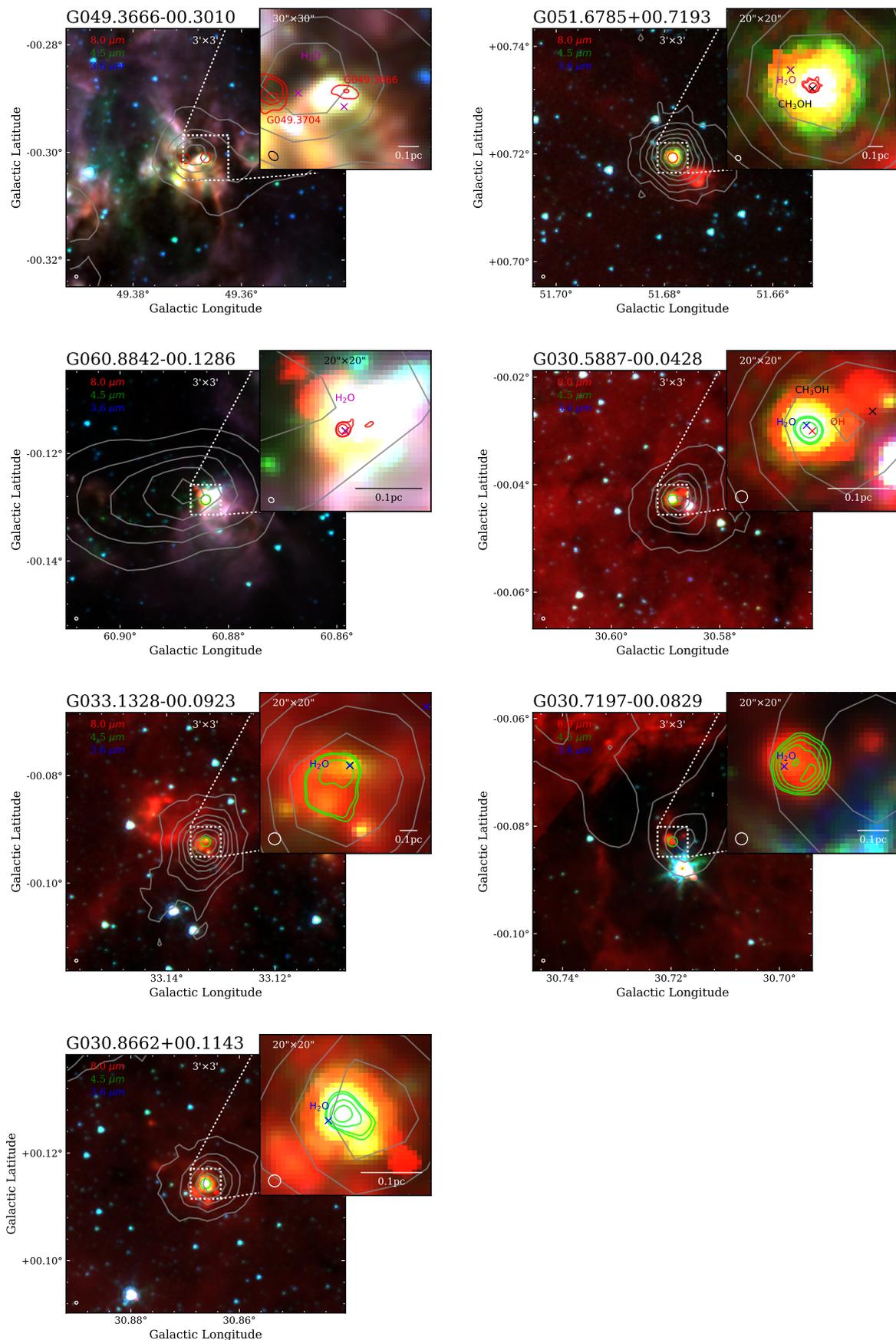
Fig. 8. As described in Fig. 6 except in this case the sources are HC H ɪɪ regions and intermediate objects between HC H ɪɪ and UC H ɪɪ regions. The grey contours in the image of G060.8842−00.1286 show the 500 μm emission from Hi−GAL. The lime contours in the images of G030.7197−00.0829, G030.8662+00.1143, G030.5887−00.0428 and G33.1328−00.0923 show the 5 GHz emission from CORNISH survey.

H39α RRL ($\Delta v = 47.8 \, \mathrm{km \, s^{-1}}$; Kim et al. 2017). Cyganowski et al. (2008) identified this source as an extended green object associated with an infrared dark cloud. The physical parameters determined for this source ($n_e = 1.02 \times 10^5 \, \mathrm{cm^{-3}}$, $diam = 0.023 \, \mathrm{pc}$, EM $= 2.36 \times 10^8 \, \mathrm{pc \, cm^{-6}}$, $\nu_t = 7.89 \, \mathrm{GHz}$) are consistent with this being classified as an HC H II region.

G061.4770+00.0892: This object is very compact with a deconvolved size similar to the beam size ($\sim 0.7''$) at K-band, and its radio emission is blended with a nearby cometary UC H II region detected both in 5 GHz CORNISH and X-band observations described in this work. However, the two sources are separated in the high resolution observations presented by Wood & Churchwell (1989) ($\sim 0.4''$) and our K-band observations ($\sim 0.7''$). As shown in the bottom-right of Fig. 7, the near-infrared RGB image of this source presents extended 4.5 μm emission and so it could be associated with an extended green object (EGO) as defined by Cyganowski et al. (2008). A bipolar molecular outflow with direction of NE−SW (Phillips & Mampaso 1991; White & Fridlund 1992) and water masers (Henkel et al. 1986; Svoboda et al. 2016), are detected toward its parent cloud. Broad RRL components (Garay et al. 1998) and strong OH (1665/67 MHz) absorption (Sarma et al. 2013) are reported towards this source and the other physical properties derived from radio emission indicate that this source is likely to host an HC H II region.

4.1.2. Intermediate objects between HC H II and UC H II regions

According to their physical properties, there are 8 objects located in the evolutionary stages between HC H II regions and UC H II regions in Table 8. Two out of the eight sources (i.e. G034.2572+00.1535 and G045.0694+00.1323) are associated with clusters of H II regions that have already been discussed in Sect. 4.1.1; in the following subsections we will provide brief notes on the other six intermediate objects.

G030.7197−00.0829: This source was resolved at 5 GHz by CORNISH. The physical properties ($n_e = 0.22 \times 10^5 \, \mathrm{cm^{-3}}$, $diam = 0.09 \, \mathrm{pc}$, EM$=0.45 \times 10^8 \, \mathrm{pc \, cm^{-6}}$, $\nu_t = 3.6 \, \mathrm{GHz}$) can be determined from the radio SED based on flux densities of 464.58 mJy at 1.4 GHz (White et al. 2005), 969.33 mJy at 5 GHz (Purcell et al. 2013), and of 570 mJy at 43 GHz (Leto et al. 2009). These results are consistent with the measurements in Leto et al. (2009). Its natal clump AGAL030.718−00.082 has a mass of $6.6 \times 10^3 \, M_\odot$, a bolometric luminosity of $5.5 \times 10^4 \, L_\odot$ (Urquhart et al. 2018), and a broad millimeter RRL H40α with $\Delta V = 43.0 \, \mathrm{km \, s^{-1}}$ (Kim et al. 2017), and is associated with CO outflows (Yang et al. 2018). Its Lyman continuum flux agrees with its bolometric luminosity, indicating a lack of dust within this H II region. Therefore, this source is suggested to be an intermediate object between HC H II and UC H II regions.

G030.8662+00.1143: The SED of this resolved source was constructed from the flux densities of 137.17 mJy at 1.4 GHz and of 255.2 mJy 5 GHz from White et al. (2005), 306.0 mJy at 6.7 GHz and 356.0 mJy 8.4 GHz from Walsh et al. (1998), as well as 560 mJy at 43 GHz from Leto et al. (2009). Its physical characteristics measured from the radio SED such as $n_e = 0.37 \times 10^5 \, \mathrm{cm^{-3}}$, $diam = 0.03 \, \mathrm{pc}$, EM$=0.42 \times 10^8 \, \mathrm{pc \, cm^{-6}}$, $\nu_t = 3.5 \, \mathrm{GHz}$ are consistent with previous measurements (Leto et al. 2009). Water masers sites (Urquhart et al. 2009a, 2011) are

detected in its vicinity and molecular outflows (Yang et al. 2018) are found to be associated with its natal clump. Its natal clump AGAL030.866+00.114 has a mass of 295 $M_\odot$, a bolometric luminosity of $1.30 \times 10^4 \, L_\odot$ (Urquhart et al. 2018), and a broad millimeter RRL H39α with $\Delta V = 44.9 \, \mathrm{km \, s^{-1}}$ (Kim et al. 2017). Its spectral type B0.5 obtained from the bolometric luminosity is consistent with O9.5 derived from radio luminosity, indicating the absence of dust in this H II region. Therefore, this source would be an intermediate object.

G033.1328−00.0923: This source shows extended emission at 5 GHz CORNISH, shown as lime contours in the bottom-left of Fig. 8. With flux densities of 173.43 mJy at 1.4 GHz and of 378.59 mJy at 5 GHz summarised in Yang et al. (2019), as well as 461.2 mJy at 9 GHz and 675.3 mJy at 15 GHz measured by Kurtz et al. (1994), we construct its radio SED between 1–15 GHz. Its physical properties from the SED fitting are consistent with results in Kurtz et al. (1994). Water masers (Pestalozzi et al. 2005; Kurtz & Hofner 2005) are detected in its vicinity and molecular outflows (Yang et al. 2018) are found to be associated with its natal clump. Its natal clump AGAL033.133−00.092 has a mass of $5.0 \times 10^3 \, M_\odot$, a bolometric luminosity of $1.1 \times 10^5 \, L_\odot$ (Urquhart et al. 2014, 2018), and a broad millimeter RRL H39α with $\Delta V = 43.0 \, \mathrm{km \, s^{-1}}$ (Kim et al. 2017). As it is only one radio source in the natal clump, its spectral type O7 obtained from the bolometric luminosity is consistent with O7.5 derived from the radio luminosity. Therefore, this source is likely to be an intermediate object between HC H II and UC H II region.

G049.3666−00.3010: This object appears to have a nearby UC H II region to the east referenced as G049.3704−00.3012 (marked with a red circle in the upper-left panel of Fig. 8). Both of these H II regions are embedded towards the center of the dense clump AGAL049.369−00.301, which has been associated with a broad H40α RRL with $\Delta V = 34.5 \, \mathrm{km \, s^{-1}}$ (Kim et al. 2017). The optically-thick radio source is coincident with an extended mid-infrared source, and two water masers have been detected in its vicinity (Valdettaro et al. 2001; Xi et al. 2015).

G051.6785+00.7193: This radio source is very compact at all radio bands presented in this work, while it can be resolved into two sources at high angular resolution $\sim 0.2''$ at 1.3 cm using the VLA in Rodríguez-Esnard et al. (2012). The radio source is embedded in a very compact and centrally condensed ATLASGAL clump AGAL051.678+00.719 with a mass of $2.88 \times 10^3 \, M_\odot$ and is associated with a very bright mid-infrared point source that has a luminosity of $1.0 \times 10^5 \, L_\odot$. The natal clump is also associated with water and methanol masers (Sridharan et al. 2002; Rodríguez-Esnard et al. 2012), and molecular outflows that is aligned with extended mid-infrared emission that has a NE-SW direction (Beuther et al. 2004), as presented in the upper-right panel of Fig. 8.

G060.8842−00.1286: This object is south-west of the two H II regions (see middle-left panel of Fig. 8) in the massive star-forming region S87IRS1 (Barsony 1989). The other being a nearby extended and weak H II region (Purcell et al. 2013) that has been resolved out at K-band in this work. The S87IRS1 is associated with the clump JPSG060.886-00.129 in Eden et al. (2017) that is itself associated with a molecular outflow (Barsony 1989; Xue & Wu 2008). The radio source is associated with

bright mid-infrared emission and coincident with a water maser (Kurtz & Hofner 2005). At high resolution ∼0.4″, the clump is found to be fragmented into multiple millimeter cores (Beuther et al. 2018). Its bolometric luminosity agrees with its radio luminosity, suggesting a lack of dust within this H II region.

4.1.3. HC H II regions not resolved in this work

In addition to the optically-thick radio sources identified in this work, we include notes on another 4 HC H II regions that have been identified in previous studies (e.g., Wood & Churchwell 1989, Sewilo et al. 2004 and Zhang et al. 2014) but are unresolved in our observations. Two of the four (G043.1652+00.0129 and G035.5781−00.0305) are unresolved mainly due to that our observations include their nearby UC H II regions as the resolution is not sufficient to resolve the emission into individual sources. The remaining two (G043.1665+00.0106 and G010.9584+0.0211) are not recovered by this work primarily because our observations include a large amount of surrounding ionised gas emission as these diffuse gas is optically thin. Therefore, the derived properties in this work represent average values for sources with co-existing emission from HC H II and nearby UC H II regions or represent a complex weighted average over the compact sources plus the surrounding diffuse ionised gas, and thus do not satisfy the criteria for being classified as HC H II regions. However, these sources have been previously identified as HC H II regions and we, therefore, include these sources in this section for completeness. The source names and derived properties are given towards the end of Table 8. Two sources (G043.1652+00.0129 and G043.1665+00.0106) in the W49A complex region have already been discussed together in Sect. 4.1.1 and so are not described again here. Images of the remaining two HC H II regions are presented in Fig. 6 and brief notes are provided below.

G010.9584+0.0221: This source is an HC H II region and is located in the western part of the G10.96+0.01 region and surrounded by more diffuse ionized gas, as suggested by Sewilo et al. (2004). Its physical properties such as $n_e = 0.36 \times 10^5$ cm^{-3}, $diam = 0.029$ pc, EM = 0.38×10^8 pc cm^{-6} and log $N_{Ly} = 47.35$, are all consistent with the results reported by Sewilo et al. (2004) and Sewiło et al. (2011). In spite of the reported broad H92α line with $\Delta V = 43.8 \pm 1.5$km s^{-1}, the derived properties are slightly below the typical values of HC H II regions, which might be due to the previous VLA observations (Sewilo et al. 2004, Sewiło et al. 2011) and this work includes a significant amount of optically thin emission from the diffuse ionised gas around this source, and both results are likely to be underestimates by averaging over the compact source plus its surrounding ionised gas, as mentioned in Sewilo et al. (2004) and Yang et al. (2019). Its natal clump has a mass of 398 $M_\odot$ and a bolometric luminosity of $1.0 \times 10^4 L_\odot$ (Urquhart et al. 2018), and is associated with high velocity outflow wings identified in CO spectra from the SEDIGISM survey (Schuller et al. 2017). In this case, the luminosity and Lyman continuum flux are both contributed by the same source, so that the spectral type derived from the bolometric luminosity is consistent with that derived from the radio luminosity; B0.5 and B0, respectively.

G035.5781−00.0305: This radio emission can be resolved into two extremely close sources at 2 cm and 3.6 cm with a resolution < 1″ (Kurtz et al. 1994): the source to the west has

been identified as an HC H II region G35.578−0.030 (Zhang et al. 2014) and the source to the east as an UC H II , G35.578−0.031 (Kurtz et al. 1994). These are seen as a single blended source in our radio maps (see the middle-right panel of Fig. 6). This source is associated with OH masers (Argon et al. 2000) and H$_2$O masers (Forster & Caswell 1999; Urquhart et al. 2011). The physical properties for the blended source G035.5781−00.0305 are $n_e = 0.22 \times 10^5$ cm^{-3}, $diam = 0.093$ pc, EM = 0.45×10^8 pc cm^{-6}, and log $N_{Ly} = 48.36$. Thus, G035.5781−00.0305 in this work has smaller n_e, smaller EM and larger $diam$ compared to the HC H II region G35.578−0.030 in Zhang et al. (2014) with $n_e = 3.3 \times 10^5$ cm^{-3}, $diam = 0.018$ pc, EM = 1.9×10^9 pc cm^{-6}. Its natal clump has a mass of $6.8 \times 10^3 M_\odot$ and a bolometric luminosity $2.0 \times 10^5 L_\odot$ (Urquhart et al. 2018), which is associated with molecular outflows (Yang et al. 2018).

4.1.4. Summary

In Table 8 we summarise the physical properties and associated discussion in the preceding text. An inspection of this table reveals that in addition to the physical properties (n_e, $diam$, EM and RRL), which are typical for HC H II regions, they are all found to be embedded towards the centres of dense molecular clumps and are also commonly associated with various masers, molecular outflows, broad RRL and extended green objects, all of which are all signposts of active star formation. The bolometric luminosities tend to be higher than the radio flux suggest, which is consistent with these being associated with a forming protocluster. These optically-thick H II regions are thus the best examples to investigate the relation between HC H II regions and UC H II regions, to study the birth of H II regions, and thus to understand the final stages of accretion in massive star formation.

There are the 13 HC H II regions, 3 HC H II region candidates and 8 intermediate objects listed in Table 8. Among them, 4 HC H II regions and 3 HC H II region candidates are newly identified by this work. Based on the classification of HC H II regions in Table 7, it is difficult to assess how complete the populations of HC H II regions and intermediate H II regions are in this work, since there are 4 HC H II regions marked with ∗ in Table 8 that are in very close proximity to other UC H II regions that have not been resolved by this work.

5. Discussion

5.1. Implications of the evolution of young H II regions

As suggested by classical theoretical models (Dyson et al. 1995; Mezger & Henderson 1967), H II regions are expected to expand over time, which results in decreasing n_e, EM and increasing $diam$, as seen in Fig. 5. The plots shown in this figure display a clear evolutionary trend in n_e, $diam$, and EM from HC H II region to the intermediate objects between the HC H II and UC H II region stages. The mean values of physical properties range from $n_e = 2.5 \times 10^5$ cm^{-3}, $diam = 0.012$ pc for HC H II region, and EM = 5.5×10^8 pc cm^{-6} to $n_e = 0.79 \times 10^5$ cm^{-3}, $diam = 0.03$, and EM = 1.58×10^8 pc cm^{-6} for intermediate objects, and thus n_e tends to change quickly compared to the EM and $diam$ in the earliest stages of H II region.

To investigate the evolution of physical properties over a wider evolutionary stages, we add the CORNISH UC H II regions from Kalcheva et al. (2018) that are presumably in a later stage compared to our sample. The evolution of the Lyman continuum flux N_{Ly}, turnover frequency ν_t, and emission measure are presented in Fig. 9 for the three subsamples discussed here
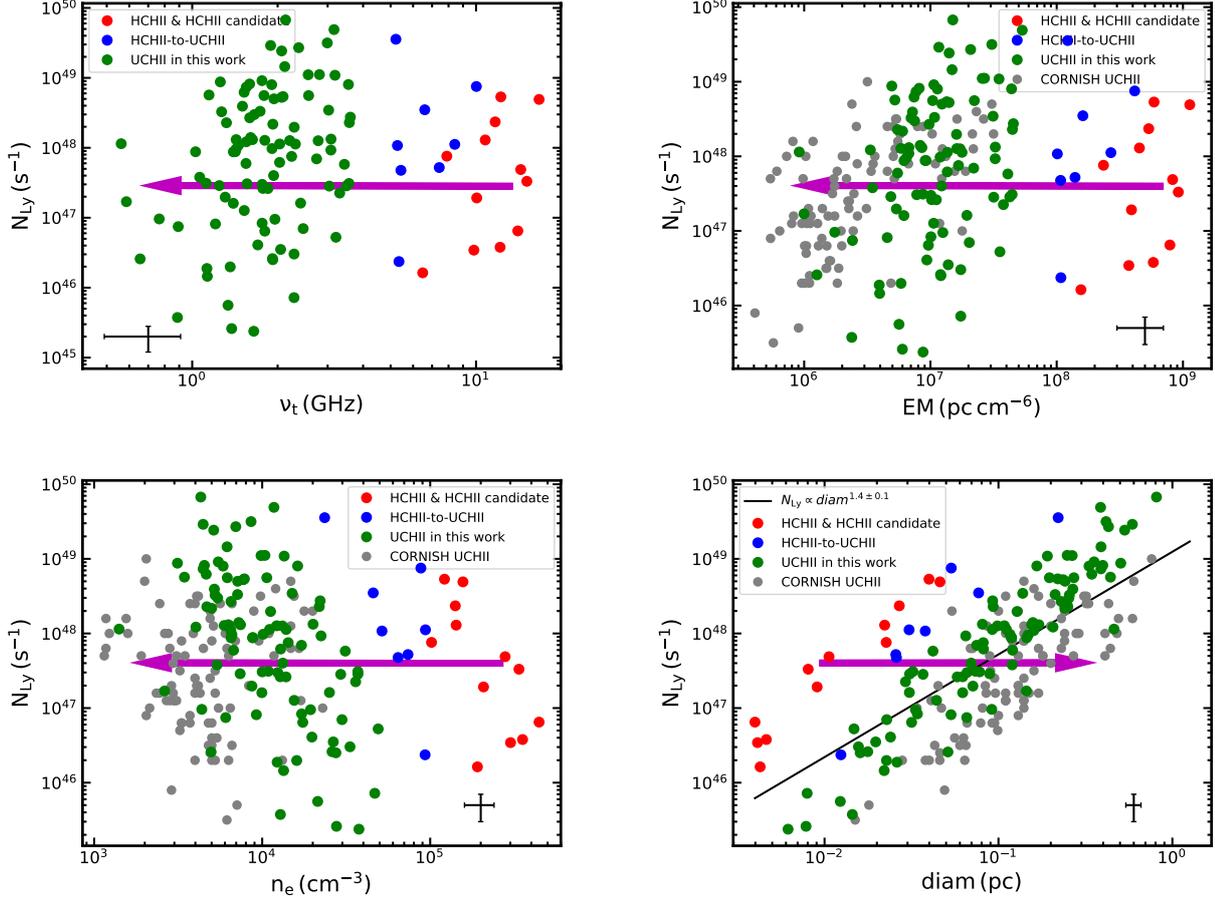
Fig. 9. The plots of turnover frequency against Lyman continuum flux N_{Ly} (upper-left), emission measure EM versus N_{Ly} (upper-right), and electron density n_e versus N_{Ly} (bottom-left), physical diameter *diam* versus Lyman continuum flux N_{Ly} (bottom-right) for HC H II regions (red dots), intermediate objects between HC H II region and UC H II regions (blue), UC H II regions in this work (green dots), and CORNISH UC H II regions (grey dots). The CORNISH UC H II regions sample refers to the whole CORNISH UC H II regions sample from Kalcheva et al. (2018) by excluding UC H II regions in this work. The magenta arrow indicates the evolutionary trend of the physical properties.

and for the four subsamples by adding the more evolved COR-NISH UC H II regions. Obviously, ν_t decreases as the H II region evolves, from 11.5 GHz for HC H II regions, to 6.4 GHz for intermediate objects, and to 1.8 GHz for UC H II regions, as expected by theoretical model in Mezger & Henderson (1967). It is interesting to note that there is no obvious correlation between the Lyman continuum flux and the evolution of the H II regions. Furthermore, we find no significant correlation between N_{Ly} and EM with $\rho = -0.01$ and *p*-value = 0.85, and between N_{Ly} and n_e with $\rho = -0.07$ and *p*-value = 0.3 in the four subsamples. In addition, the mean values of $N_{Ly} \sim 10^{48}$ s^{-1} is consistent among the four evolutionary phases from the HC H II region and HC H II region candidates, to intermediate objects, to UC H II regions in this work, and to more evolved UC H II regions in CORNISH. These results suggest that there is effectively no evolution of the Lyman continuum photon flux with changes in the turnover frequency, electron density as well as emission measure, and by extension there is no increase in N_{Ly} with evolution of the H II region.

As shown in the bottom-left of Fig. 9, the positive correlation between N_{Ly} and *diam* is significant with $\rho = 0.5$ and *p*-value $\ll 0.001$ by using a partial correlation test to control the distance dependence, giving a power-law relation $N_{Ly} \propto diam^{1.4\pm0.1}$. However, given the fact that there is little evidence of any sort

of significant correlations between Lyman continuum flux and other parameters tracing the evolution of H II regions, such as ν_t, n_e and EM as discussed before, this correlation is more likely to result from the fact that more luminous H II regions expand more rapidly in their early stages but that the expansion speed will decrease over time to be similar to less luminous H II regions. The evolution in this plot is therefore from left to right rather than diagonal from bottom-left to upper-right as suggested from the distribution. The flat evolution of N_{Ly} indicates that the value of N_{Ly} remains constant as the H II region develops, and by extension that the ionizing flux from a young massive star remains constant during the evolutionary phases of H II regions in this sample. This result agrees with the classical expansion model without gravity or the model with gravity in Keto (2002) in which the N_{Ly} of H II region tends to stop increasing if it reaches the critical radios where the accretion is quickly reduced. Also, the constant N_{Ly} over time agrees with the results of Hosokawa & Omukai (2009) and Hosokawa et al. (2010) who showed that the luminosity and temperature of a bloated protostar remain almost unchanged in the last accretion phase. Moreover, the almost unchanged N_{Ly} may also support the model of Peters et al. (2010) who proposed that a shrinking H II region has small fluctuations of 5%7% in ionizing flux over time.
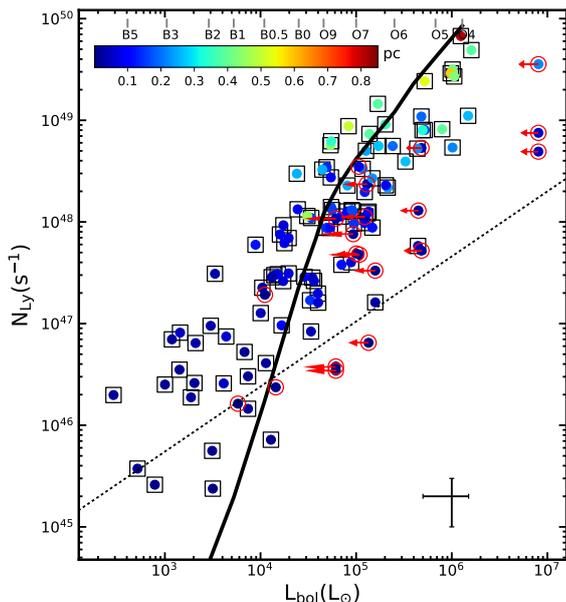
Fig. 10. Lyman continuum flux N_{Ly} versus the bolometric luminosity L_{bol} for young H II regions with rising spectra. The black solid line refers to the expected Lyman continuum photon rate from a single Zero-age main-sequence (ZAMS) star of a given bolometric luminosity. The top axis lists the spectral type corresponding to a given bolometric luminosity, taken from stellar models (Thompson 1984; Panagia 1973; Davies et al. 2011). The error bars in the bottom right corner correspond to a 50% uncertainty for L_{bol} and N_{Ly} (Urquhart et al. 2018). At the top, we show the color bar for the source physical size, indicating the physical diameter in pc. The red circles and black squares refer to optically-thick H II regions ($\nu_t > 5$ GHz) and optically-thin H II regions ($\nu_t < 5$ GHz). About 30% of the sample is located in the forbidden region above the solid curve considering a 50% uncertainty. The dotted line represents the empirical relation between L_{bol} and N_{Ly} for ionized jets from YSOs, with a power-law index 0.64 derived by Purser et al. (2016). The red arrows for the optically-thick H II regions indicate that the bolometric luminosities are upper limits due to the presence of other H II regions in the same clump.

5.2. Lyman continuum–bolometric luminosity relationship

The measurements of Lyman continuum flux in the optically-thin regime presented in Sect. 3.3.2 and the bolometric luminosity of the sample measured by previous studies (see Table 1) allow us to discuss the relation between Lyman continuum photons (N_{Ly}) and bolometric luminosity (L_{bol}), as well as Lyman continuum flux excess phenomenon in the young H II regions sample. There exists a significantly positive correlation between L_{bol} and N_{Ly} with $\rho = 0.54$ and p-value $\ll 0.001$ by using the partial correlation test to remove the distance dependence, which is consistent with the correlation ($\rho = 0.69$) calculated by Urquhart et al. (2013) for a sample of ultra-compact and compact H II regions.

Fig. 10 shows N_{Ly} as a function of L_{bol}. The color symbols indicate the physical size of the sample and the black solid line represents to the upper limit of the expected Lyman continuum photon rates at specific given bolometric luminosities for zero-age main-sequence (ZAMS) stars. About 40% of the sources in the sample are located in the forbidden region above this black line, suggesting a Lyman continuum excess. Considering a 50% uncertainty on N_{Ly} and L_{bol}, the fraction of Lyman excess

sources in our sample is consistent with ~30% sources in previous work (Sánchez-Monge et al. 2013; Cesaroni et al. 2015). Those sources with Lyman excess are more likely to be associated with young B-type stars (e.g., Sánchez-Monge et al. 2013; Lumsden et al. 2013; Urquhart et al. 2013).

Most of the optically-thick H II regions in the sample do not show a Lyman continuum excess; these are marked with red circles in Fig. 10 and located to the right of the black solid line representing the upper limit of the expected Ly continuum photons. The primary reason for this is that many are embedded in clusters (as discussed in Sect. 4). Although it is possible that the Lyman flux has been underestimated due to filtering of some of the extended flux in the interferometric observations (e.g., Urquhart et al. 2013), and due to absorption by dust in the H II region (e.g., Wood & Churchwell 1989; Garay et al. 1993), it is unlikely these affects would be significant enough to result in these objects having a Lyman excess (in many cases the Lyman flux would need to have been underestimated by an order of magnitude or more).

It is possible that some of the optically-thick objects we have detected are ionized jets, whose radio emission also has positive spectral indices (Moscadelli et al. 2016; Purser et al. 2016), and since there are very weak ($S_{int} \sim$ mJy) and compact (*diam* ~ 1000 AU) sources (see Sect. 4). We have included the empirical relationship between bolometric luminosity (L_{bol}) and Lyman flux (N_{Ly}) derived from young stellar objects (YSOs) on Fig. 10 (dotted diagonal line; Purser et al. 2016). Given that it is likely that the Lyman continuum flux has been underestimated and the bolometric luminosity has been overestimated, then only the optically thick sources located to the right of this relation are associated with radio jets; these are G030.0096, G060.8842, G034.2573, G034.2581, G061.4770. The radio emission of the five sources are point-like as shown in Fig. 7 and Fig. 8, and thus no morphological evidence was were found to indicate that they are radio jets, which implies that they are more likely to be HC H II regions as discussed in Sect. 4. Further observations are needed to reliably classify these objects.

In Fig. 10, there are seven young H II regions in Table 8 located close to the black solid line, such as G010.9584, G030.0096, G030.5887, G030.8662, G060.8842, G030.7197, and G033.1328, which means that their Lyman continuum fluxes agree well with their bolometric luminosities, and further indicates that the absence of dust within these H II regions to absorb the Lyman continuum photons. All of the seven objects are the only radio source in observed field of this work and in their parent clumps from Urquhart et al. (2018). Three of the seven (G010.9584, G030.0096, and G030.5887) are suggested to be in the HC H II region stage and the remaining four are expected to be in the intermediate stage between HC H II regions and UC H II regions. Except for three sources with no RRL information, the rest five sources show broad RRL with line widths $\Delta V > 40$ km s^{-1}, and all of them are associated with outflows and masers, as shown in Table 8. These dust-free and young H II regions are interesting cases to study the destruction of dust in the very young H II regions since H II regions are often expected to be dusty in the early stages, as discussed in Sect. 3.3.3 and in Arthur et al. (2004). Further investigations are needed to understand the absence of dust in these young H II regions.

6. Summary and conclusion

In this work, we reported the results of multi-band (8–12 GHz and 18–26 GHz), high angular-resolution (~ 1.7″ and ~ 0.7″), VLA observations toward a sample of young H II regions that are selected on the basis of rising spectra between 1–5 GHz in Yang

et al. (2019). We construct their radio SED between 1 GHz and 26 GHz and measure their physical properties for 116 young H ɪɪ regions by modelling each SED based on an ionisation-bounded H ɪɪ region with standard uniform electron density. The sample has a mean electron density of $n_e = 1.6 \times 10^4\,\mathrm{cm^{-3}}$, a mean diameter of $diam = 0.14\,\mathrm{pc}$, a mean emission measure of EM= $1.9 \times 10^7\,pc\,cm^{-6}$, a mean turnover frequency of $\nu_t = 3.29\,\mathrm{GHz}$, and a mean Lyman continuum flux of $N_{Ly} = 6.5 \times 10^{47}\,s^{-1}$. Based on these properties, there are in total 20 HC H ɪɪ regions and 3 candidates reported so far after combining with HC H ɪɪ region catalog summarised in Yang et al. (2019). This sample consists of a large number of HC H ɪɪ regions and UC H ɪɪ regions, which gives us a comprehensive picture of the physical condition and evolution of these young H ɪɪ regions. The main results are summarised as follows:

1. We identify 16 HC H ɪɪ regions and 8 intermediate objects located between the class of HC H ɪɪ and UC H ɪɪ regions. 4 HC H ɪɪ regions and 3 candidates are newly reported in this work, with two new infrared dark HC H ɪɪ region detection.

2. We have discussed how the physical properties of H ɪɪ regions change as they evolve from HC H ɪɪ region to UC H ɪɪ region and then to compact H ɪɪ region. While the n_e, $diam$, EM, and ν_t all change during the evolution, the Lyman continuum flux is relatively constant over time. This suggest that the accretion tends to be quickly reduced or could be halted at the earliest HC H ɪɪ region stage in our sample.

3. These young and compact H ɪɪ regions are located in dusty clumps. The mean fraction of ionizing flux absorbed by dust in H ɪɪ regions is 67%, and the absorption fraction tends to be more significant for the more compact and presumably younger H ɪɪ regions. Even though, about 40% of the sources show Lyman continuum excess and they are preferentially associated with young B-type stars.

In conclusion, a young H ɪɪ region is likely to be located in dusty clump. The youngest H ɪɪ regions such as HC H ɪɪ regions and intermediate objects between HC H ɪɪ and UC H ɪɪ regions are found to be associated with star-forming activities such as various masers, molecular outflows, broad RRL and extended green objects, and the accretion at the two stages tends to be quickly reduced or stopped, and thus that they could be optimal tracers of the final stages in massive star formation.

References

Afflerbach, A., Churchwell, E., Acord, J. M., et al. 1996, ApJS, 106, 423
Argon, A. L., Reid, M. J., & Menten, K. M. 2000, ApJS, 129, 159
Arthur, S. J., Kurtz, S. E., Franco, J., & Albarrán, M. Y. 2004, ApJ, 608, 282
Avalos, M., Lizano, S., Rodríguez, L. F., Franco-Hernández, R., & Moran, J. M. 2006, ApJ, 641, 406
Barsony, M. 1989, ApJ, 345, 268
Bartkiewicz, A., Szymczak, M., & van Langevelde, H. J. 2014, A&A, 564, A110
Bartkiewicz, A., Szymczak, M., & van Langevelde, H. J. 2016, A&A, 587, A104
Battersby, C., Bally, J., Ginsburg, A., et al. 2011, A&A, 535, A128
Beltrán, M. T., Cesaroni, R., Moscadelli, L., & Codella, C. 2007, A&A, 471, L13
Beltrán, M. T., Cesaroni, R., Zhang, Q., et al. 2011, A&A, 532, A91
Benjamin, R. A., Churchwell, E., Babler, B. L., et al. 2003, PASP, 115, 953
Beuther, H., Bihr, S., Rugel, M., et al. 2016, A&A, 595, A32
Beuther, H., Mottram, J. C., Ahmadi, A., et al. 2018, A&A, 617, A100
Beuther, H., Schilke, P., & Gueth, F. 2004, ApJ, 608, 330
Bihr, S., Johnston, K. G., Beuther, H., et al. 2016, A&A, 588, A97
Bisbas, T. G., Haworth, T. J., Williams, R. J. R., et al. 2015, MNRAS, 453, 1324
Blum, R. D., Damineli, A., & Conti, P. S. 1999, AJ, 117, 1392
Breen, S. L., Fuller, G. A., Caswell, J. L., et al. 2015, MNRAS, 450, 4109
Carey, S. J., Noriega-Crespo, A., Mizuno, D. R., et al. 2009, PASP, 121, 76
Caswell, J. L., Batchelor, R. A., Forster, J. R., & Wellington, K. J. 1983, Australian Journal of Physics, 36, 443
Caswell, J. L., Green, J. A., & Phillips, C. J. 2013, MNRAS, 431, 1180
Cesaroni, R., Beltrán, M. T., Moscadelli, L., Sánchez-Monge, Á., & Neri, R. 2019, A&A, 624, A100
Cesaroni, R., Pestalozzi, M., Beltrán, M. T., et al. 2015, A&A, 579, A71
Churchwell, E., Babler, B. L., Meade, M. R., et al. 2009, PASP, 121, 213
Codella, C., Beltrán, M. T., Cesaroni, R., et al. 2013, A&A, 550, A81
Contreras, Y., Schuller, F., Urquhart, J. S., et al. 2013, A&A, 549, A45
Csengeri, T., Leurini, S., Wyrowski, F., et al. 2016, A&A, 586, A149
Cyganowski, C. J., Whitney, B. A., Holden, E., et al. 2008, AJ, 136, 2391
Davies, B., Hoare, M. G., Lumsden, S. L., et al. 2011, MNRAS, 416, 972
de Pree, C. G., Gaume, R. A., Goss, W. M., & Claussen, M. J. 1996, ApJ, 464, 788
De Pree, C. G., Mehringer, D. M., & Goss, W. M. 1997, ApJ, 482, 307
De Pree, C. G., Wilner, D. J., Goss, W. M., Welch, W. J., & McGrath, E. 2000, ApJ, 540, 308
De Pree, C. G., Wilner, D. J., Mercer, A. J., et al. 2004, ApJ, 600, 286
Djordjevic, J. O., Thompson, M. A., Urquhart, J. S., & Forbrich, J. 2019, MNRAS, 487, 1057
Dyson, J. E. & Williams, D. A. 1997, The physics of the interstellar medium, 2nd edn. (Bristol and Philadelphia: Institute of Physics Publishing)
Dyson, J. E., Williams, R. J. R., & Redman, M. P. 1995, MNRAS, 277, 700
Eden, D. J., Moore, T. J. T., Plume, R., et al. 2017, MNRAS, 469, 2163
Ellingsen, S. P., Breen, S. L., Sobolev, A. M., et al. 2011, ApJ, 742, 109
Forster, J. R. & Caswell, J. L. 1999, A&AS, 137, 43
Forster, J. R. & Caswell, J. L. 2000, ApJ, 530, 371
Fu, L. & Lin, G.-M. 2016, Research in Astronomy and Astrophysics, 16, 182
Furuya, R. S., Cesaroni, R., Codella, C., et al. 2002, A&A, 390, L1
Gao, X. Y., Reich, P., Hou, L. G., Reich, W., & Han, J. L. 2019, A&A, 623, A105
Garay, G. & Lizano, S. 1999, PASP, 111, 1049
Garay, G., Lizano, S., Gómez, Y., & Brown, R. L. 1998, ApJ, 501, 710
Garay, G., Rodriguez, L. F., Moran, J. M., & Churchwell, E. 1993, ApJ, 418, 368
Gibb, A. G. & Hoare, M. G. 2007, MNRAS, 380, 246
Hatchell, J., Thompson, M. A., Millar, T. J., & MacDonald, G. H. 1998, A&AS, 133, 29
Helfand, D. J., Becker, R. H., White, R. L., Fallon, A., & Tuttle, S. 2006, AJ, 131, 2525
Henkel, C., Haschick, A. D., & Guesten, R. 1986, A&A, 165, 197
Hoare, M. G., Kurtz, S. E., Lizano, S., Keto, E., & Hofner, P. 2007, Protostars and Planets V, 181
Hoare, M. G., Purcell, C. R., Churchwell, E. B., et al. 2012, PASP, 124, 939
Hofner, P. & Churchwell, E. 1996, A&AS, 120, 283
Hollenbach, D., Johnstone, D., Lizano, S., & Shu, F. 1994, ApJ, 428, 654
Hosokawa, T. & Omukai, K. 2009, ApJ, 691, 823
Hosokawa, T., Yorke, H. W., & Omukai, K. 2010, ApJ, 721, 478
Imai, H., Omi, R., Kurayama, T., et al. 2011, PASJ, 63, 1293
Kalcheva, I. E., Hoare, M. G., Urquhart, J. S., et al. 2018, A&A, 615, A103
Keto, E. 2002, ApJ, 580, 980
Keto, E. 2003, ApJ, 599, 1196
Keto, E. 2007, ApJ, 666, 976
Keto, E. & Wood, K. 2006, ApJ, 637, 850
Keto, E., Zhang, Q., & Kurtz, S. 2008, ApJ, 672, 423
Kim, H.-D., Cho, S.-H., Chung, H.-S., et al. 2000, ApJS, 131, 483
Kim, K.-T. & Koo, B.-C. 2001, ApJ, 549, 979
Kim, W. J., Urquhart, J. S., Wyrowski, F., Menten, K. M., & Csengeri, T. 2018, A&A, 616, A107
Kim, W.-J., Wyrowski, F., Urquhart, J. S., Menten, K. M., & Csengeri, T. 2017, A&A, 602, A37
König, C., Urquhart, J. S., Csengeri, T., et al. 2017, A&A, 599, A139
Kurtz, S. 2005, in IAU Symposium, Vol. 227, Massive Star Birth: A Crossroads of Astrophysics, ed. R. Cesaroni, M. Felli, E. Churchwell, & M. Walmsley, 111–119
Kurtz, S., Cesaroni, R., Churchwell, E., Hofner, P., & Walmsley, C. M. 2000, Protostars and Planets IV, 299
Kurtz, S., Churchwell, E., & Wood, D. O. S. 1994, ApJS, 91, 659
Kurtz, S. & Hofner, P. 2005, AJ, 130, 711
Kurtz, S., Hofner, P., & Álvarez, C. V. 2004, ApJS, 155, 149
Leto, P., Umana, G., Trigilio, C., et al. 2009, A&A, 507, 1467
López-Sepulcre, A., Codella, C., Cesaroni, R., Marcelino, N., & Walmsley, C. M. 2009, A&A, 499, 811
Lumsden, S. L., Hoare, M. G., Urquhart, J. S., et al. 2013, ApJS, 208, 11
Maud, L. T., Moore, T. J. T., Lumsden, S. L., et al. 2015, MNRAS, 453, 645
McKee, C. F. & Tan, J. C. 2003, ApJ, 585, 850

McMullin, J. P., Waters, B., Schiebel, D., Young, W., & Golap, K. 2007, Astronomical Society of the Pacific Conference Series, Vol. 376, CASA Architecture and Applications, ed. R. A. Shaw, F. Hill, & D. J. Bell, 127

Medina, S. N. X., Urquhart, J. S., Dzib, S. A., et al. 2019, A&A, 627, A175

Mezger, P. G. & Henderson, A. P. 1967, ApJ, 147, 471

Molinari, S., Swinyard, B., Bally, J., et al. 2010, PASP, 122, 314

Moscadelli, L., Sánchez-Monge, Á., Goddi, C., et al. 2016, A&A, 585, A71

Motte, F., Bontemps, S., & Louvet, F. 2018, ARA&A, 56, 41

Murphy, T., Cohen, M., Ekers, R. D., et al. 2010, MNRAS, 405, 1560

Panagia, N. 1973, AJ, 78, 929

Panagia, N. & Felli, M. 1975, A&A, 39, 1

Pascucci, I., Apai, D., Henning, T., Stecklum, B., & Brandl, B. 2004, A&A, 426, 523

Pestalozzi, M. R., Minier, V., & Booth, R. S. 2005, A&A, 432, 737

Peters, T., Banerjee, R., Klessen, R. S., et al. 2010, ApJ, 711, 1017

Phillips, J. P. & Mampaso, A. 1991, A&AS, 88, 189

Purcell, C. R., Hoare, M. G., Cotton, W. D., et al. 2013, ApJS, 205, 1

Purser, S. J. D., Lumsden, S. L., Hoare, M. G., et al. 2016, MNRAS, 460, 1039

Rodríguez-Esnard, T., Trinidad, M. A., & Migenes, V. 2012, ApJ, 761, 158

Ruiz-Velasco, A. E., Felli, D., Migenes, V., & Wiggins, B. K. 2016, ApJ, 822, 101

Sánchez-Monge, Á., Beltrán, M. T., Cesaroni, R., et al. 2013, A&A, 550, A21

Sarma, A. P., Brogan, C. L., Bourke, T. L., Eftimova, M., & Troland, T. H. 2013, ApJ, 767, 24

Schlingman, W. M., Shirley, Y. L., Schenk, D. E., et al. 2011, ApJS, 195, 14

Schuller, F., Csengeri, T., Urquhart, J. S., et al. 2017, A&A, 601, A124

Schuller, F., Menten, K. M., Contreras, Y., et al. 2009, A&A, 504, 415

Scoville, N. Z., Sargent, A. I., Sanders, D. B., et al. 1986, ApJ, 303, 416

Sewilo, M., Churchwell, E., Kurtz, S., Goss, W. M., & Hofner, P. 2004, ApJ, 605, 285

Sewiło, M., Churchwell, E., Kurtz, S., Goss, W. M., & Hofner, P. 2011, ApJS, 194, 44

Shirley, Y. L., Ellsworth-Bowers, T. P., Svoboda, B., et al. 2013, ApJS, 209, 2

Spitzer, L. 1978, Physical processes in the interstellar medium (WILEY-VCH Verlag GmbH & Co. KGaA)

Sridharan, T. K., Beuther, H., Schilke, P., Menten, K. M., & Wyrowski, F. 2002, ApJ, 566, 931

Steggles, H. G. 2016, PhD thesis, University of Leeds

Steggles, H. G., Hoare, M. G., & Pittard, J. M. 2017, MNRAS, 466, 4573

Surcis, G., Vlemmings, W. H. T., van Langevelde, H. J., et al. 2015, A&A, 578, A102

Svoboda, B. E., Shirley, Y. L., Battersby, C., et al. 2016, ApJ, 822, 59

Thompson, M., Beuther, H., Dickinson, C., et al. 2015, Advancing Astrophysics with the Square Kilometre Array (AASKA14), 126

Thompson, M., Goedhart, S., Goedhart, S., et al. 2016, in MeerKAT Science: On the Pathway to the SKA, 15

Thompson, M. A., Hatchell, J., Walsh, A. J., MacDonald, G. H., & Millar, T. J. 2006, A&A, 453, 1003

Thompson, R. I. 1984, ApJ, 283, 165

Urquhart, J. S., Busfield, A. L., Hoare, M. G., et al. 2007, A&A, 461, 11

Urquhart, J. S., Csengeri, T., Wyrowski, F., et al. 2014, A&A, 568, A41

Urquhart, J. S., Hoare, M. G., Lumsden, S. L., et al. 2009a, A&A, 507, 795

Urquhart, J. S., Hoare, M. G., Purcell, C. R., et al. 2009b, A&A, 501, 539

Urquhart, J. S., König, C., Giannetti, A., et al. 2018, MNRAS, 473, 1059

Urquhart, J. S., Morgan, L. K., Figura, C. C., et al. 2011, MNRAS, 418, 1689

Urquhart, J. S., Thompson, M. A., Moore, T. J. T., et al. 2013, MNRAS, 435, 400

Valdettaro, R., Palla, F., Brand, J., et al. 2001, A&A, 368, 845

van der Tak, F. F. S. & Menten, K. M. 2005, A&A, 437, 947

van der Tak, F. F. S., Shipman, R. F., Jacq, T., et al. 2019, A&A, 625, A103

Walsh, A. J., Burton, M. G., Hyland, A. R., & Robinson, G. 1998, MNRAS, 301, 640

White, G. J. & Fridlund, C. V. M. 1992, A&A, 266, 452

White, R. L., Becker, R. H., & Helfand, D. J. 2005, AJ, 130, 586

Wood, D. O. S. & Churchwell, E. 1989, ApJS, 69, 831

Wyrowski, F., Güsten, R., Menten, K. M., et al. 2016, A&A, 585, A149

Xi, H., Zhou, J., Esimbek, J., et al. 2015, MNRAS, 453, 4203

Xue, R. & Wu, Y. 2008, ApJ, 680, 446

Yang, A. Y., Thompson, M. A., Tian, W. W., et al. 2019, MNRAS, 482, 2681

Yang, A. Y., Thompson, M. A., Urquhart, J. S., & Tian, W. W. 2018, ApJS, 235, 3

Zhang, C.-P., Wang, J.-J., Xu, J.-L., Wyrowski, F., & Menten, K. M. 2014, ApJ, 784, 107

Zinnecker, H. & Yorke, H. W. 2007, ARA&A, 45, 481

Appendix A: Additional Tables

Table A.1. The sample of 118 rising-spectra H II regions

Name	$S_{1.4\,GHz}$ (mJy)	$S_{5\,GHz}$ (mJy)	Dist (kpc)	$\log L_{bol}$ ($L_\odot$)	[Ref.]	Name	$S_{1.5\,GHz}$ (mJy)	$S_{5\,GHz}$ (mJy)	Dist (kpc)	$\log L_{bol}$ ($L_\odot$)	[Ref.]
	±10%	±10%	±10%	±20%			±10%	±10%	±10%	±20%	
G010.3009−00.1477	426.2	631.4	3.5	5.2	[1]	G027.3644−00.1657	45.0	60.1	8.0	4.8	[1]
G010.4724+00.0275	31.3	38.4	8.5	5.7	[1]	G027.9782+00.0789	89.3	124.0	4.8	4.2	[2]
G010.6223−00.3788†	327.6	483.3	2.4	5.7	[1]	G028.2003−00.0494	−	161.0	6.1	5.1	[1]
G010.6234−00.3837	571.3	1952.2	5.0	5.7	[1]	G028.2879−00.3641	410.9	552.8	11.6	5.9	[1]
G010.9584+00.0221	47.9	196.0	2.9	4.0	[1]	G028.6082+00.0185	168.2	210.2	7.4	5.0	[1]
G011.0328+00.0274	3.7	5.7	2.9	2.7	[1]	G029.9559−00.0168	1610.8	3116.2	5.2	5.7	[1]
G011.1104−00.3985	253.2	305.4	5.0	4.7	[1]	G030.0096−00.2734	0.3	4.5	5.2	3.8	[1]
G011.1712−00.0662	83.2	102.2	2.9	3.2	[1]	G030.5353+00.0204	553.6	710.4	2.7	3.9	[1]
G011.9368−00.6158	735.6	1155.9	3.4	4.8	[1]	G031.0495+00.4697	10.7	13.6	2.0	3.5	[1]
G011.9446−00.0369	251.1	943.6	3.1	4.3	[1]	G031.1596+00.0448	20.7	23.8	2.7	3.3	[1]
G012.1988−00.0345	47.6	62.7	11.9	5.0	[1]	G031.2801+00.0632	144.5	268.9	5.2	4.8	[1]
G012.2081−00.1019	127.9	207.9	13.4	5.5	[1]	G032.4727+00.2036	56.0	97.4	3.0	3.5	[1]
G012.4294−00.0479	24.4	45.2	2.6	3.2	[1]	G032.7441−00.0755	0.3	7.9	11.7	5.0	[1]
G012.8050−00.2007	4332.2	12616.4	2.6	−	[1]	G032.7966+00.1909	1698.9	3123.4	13.0	6.1	[1]
G012.8131−00.1976†	907.7	1500.4	−	−	[1]	G032.9273+00.6060	229.5	285.6	15.1	4.7	[1]
G012.9995−00.3583	10.5	20.1	1.3	2.9	[1]	G033.4163−00.0036	57.6	75.2	5.4	4.1	[1]
G013.2099−00.1428	437.9	946.8	2.6	4.2	[1]	G033.9145+00.1105	464.7	842.2	6.5	5.2	[1]
G013.3850+00.0684	139.2	603.9	1.9	3.5	[1]	G034.2572+00.1535	370.8	1762.6	1.6	4.8	[1]
G014.7785−00.3328	15.4	18.2	3.1	3.0	[1]	G034.2581+00.1533	−	35.9	1.6	4.8	[1]
G016.1448+00.0088	8.8	14.8	12.3	4.2	[1]	G034.4032+00.2277	5.3	8.9	1.6	3.5	[1]
G016.3913−00.1383	40.8	124.3	1.9	2.5	[1]	G035.0242+00.3502	5.3	11.4	2.3	4.1	[1]
G016.9445−00.0738	258.5	519.3	15.9	5.2	[1]	G035.4669+00.1394	235.1	317.6	8.5	5.3	[1]
G017.0299−00.0696	2.0	5.4	10.1	4.1	[1]	G035.5781−00.0305	38.0	187.8	10.4	5.3	[1]
G017.1141−00.1124	14.2	17.2	10.1	4.5	[1]	G036.4057+00.0226	17.3	22.3	3.5	3.9	[1]
G018.1460−00.2839†	151.2	856.2	−	−	[1]	G037.5457−00.1120	252.3	406.5	9.7	5.1	[1]
G018.3024−00.3910	846.8	1277.9	3.2	4.7	[1]	G037.7347−00.1128	12.3	16.0	9.7	4.6	[1]
G018.4433−00.0056	56.2	81.3	11.9	4.5	[2]	G037.7633−00.2167†	295.3	337.6	−	−	[1]
G018.4614−00.0038	128.2	342.1	11.8	5.4	[1]	G037.8731−00.3996	1279.3	2561.2	9.7	5.7	[1]
G018.6654+00.0294	3.7	5.7	10.1	4.5	[1]	G037.9723−00.0965	10.2	20.9	16.6	4.3	[2]
G018.7106+00.0002	41.0	107.5	2.4	3.1	[1]	G038.8756+00.3080	191.2	311.3	14.2	4.7	[1]
G018.7612+00.2630	26.4	51.4	14.1	5.1	[1]	G039.1956+00.2255	14.2	62.3	14.5	4.4	[1]
G018.8250−00.4675	9.1	11.4	5.0	3.6	[1]	G039.7277−00.3973†	112.3	133.3	−	−	[1]
G018.8338−00.3002	108.4	131.4	12.7	4.9	[1]	G039.8824−00.3460	247.0	276.9	9.3	4.6	[1]
G019.0754−00.2874	333.7	380.7	5.0	5.1	[1]	G042.4345−00.2605	38.5	83.7	4.4	4.0	[1]
G019.4912+00.1352	269.3	415.1	13.7	5.1	[1]	G043.1651−00.0283	564.3	2714.3	11.1	6.2	[1]
G019.6087−00.2351	855.6	2900.9	12.6	6.0	[1]	G043.1652+00.0129	−	160.1	11.1	6.9	[1]
G019.6090−00.2313	126.5	259.9	12.6	6.0	[1]	G043.1657+00.0116	−	98.2	11.1	6.9	[1]
G019.7407+00.2821	44.4	239.0	14.0	4.7	[1]	G043.1665+00.0106	237.8	1365.7	11.1	6.9	[1]
G019.7549−00.1282	10.6	36.5	7.8	4.5	[1]	G043.1778−00.5181	122.9	181.7	8.0	5.0	[1]
G020.0720−00.1421†	138.1	210.1	−	−	[1]	G045.0694+00.1323	17.9	46.2	8.0	5.7	[1]
G020.0809−00.1362	104.4	498.2	12.6	5.7	[1]	G045.0712+00.1321	61.6	146.7	8.0	5.7	[1]
G020.3633−00.0136	32.2	55.1	3.4	3.3	[1]	G045.1223+00.1321	1346.0	2984.3	8.0	6.0	[1]
G021.3571−00.1766	18.5	24.9	10.0	4.6	[1]	G045.4545+00.0591	492.5	1029.5	6.9	5.6	[2]
G021.3855−00.2541	51.1	113.9	10.0	4.9	[1]	G045.4656+00.0452	28.9	62.3	6.6	5.0	[2]
G021.4257−00.5417	78.9	94.8	3.5	4.2	[1]	G045.4790+00.1294	380.2	504.2	6.0	4.5	[2]
G023.2654+00.0765	55.6	88.6	5.9	4.3	[1]	G048.6057+00.0228	6.6	36.2	10.8	5.6	[1]
G023.4553−00.2010	2.9	14.4	5.9	3.8	[1]	G048.6099+00.0270	56.5	131.2	9.8	5.1	[4]
G024.5065−00.2224	153.7	205.6	5.8	4.7	[1]	G048.9296−00.2793	66.9	185.4	5.6	4.2	[2]
G024.7898+00.0833	−	12.5	6.4	5.2	[1]	G049.2679−00.3374	64.4	102.6	5.6	4.5	[2]
G024.9237+00.0777†	57.1	172.5	12.2	−	[1]	G049.3704−00.3012	252.9	414.4	5.4	5.1	[3]
G025.3948+00.0332	203.7	296.9	15.6	5.3	[1]	G049.4905−00.3688	1165.6	3821.7	5.3	6.2	[1]
G025.3970+00.5614	93.7	121.2	13.9	5.1	[1]	G050.3152+00.6762	38.7	81.3	1.8	3.3	[1]
G025.3981−00.1411	1351.5	2132.2	10.2	6.0	[1]	G051.6785+00.7193	2.8	22.6	10.9	5.0	[1]
G025.7157+00.0487	15.7	20.8	9.4	4.6	[1]	G052.7533+00.3340	264.0	386.0	9.0	4.4	[2]
G025.8011−00.1568	19.2	31.9	10.2	4.9	[1]	G053.9589+00.0320	40.8	46.0	4.0	3.6	[1]
G026.5444+00.4169	301.0	413.4	9.8	5.2	[1]	G060.8842−00.1286	−	18.7	2.5	4.2	[2]
G027.2800+00.1447	370.4	428.0	13.4	4.9	[1]	G061.4763+00.0892	252.7	718.7	4.1	5.1	[2]
G030.5887−00.0428★	7.9	92.37	2.7	4.0	[1]	G030.8662+00.1143★	137.17	255.2	2.7	4.1	[1]
G030.7197−00.0829★	464.58	969.33	5.2	4.7	[1]	G033.1328−00.0923★	173.43	378.59	9.4	5.0	[1]

Notes. † refers to the sources in our observation with bad images. ★ refers to the 4 sources with data from archive and literature. Columns: (1) source name; (2) and (3) flux density at 1.4 GHz and 5 GHz taken from Yang et al. (2019); (4) heliocentric distance; (5) bolometric luminosity; (6) The reference for heliocentric distance and bolometric luminosity [1] Urquhart et al. (2018), [2] Cesaroni et al. (2015), [3] Urquhart et al. (2013), [4] Kalcheva et al. (2018). The symbol ±10% refers to an overall estimation of the percentage error at 1.4 GHz and 5 GHz.

Table A.2. Observation results of 112 young H ɪɪ regions at X-band (8–12 GHz) and K-band (18–26 GHz).

Name	$S_{Peak}(X)$ (mJy/beam)	$\sigma(X)$ (mJy)	$S_{9\,GHz}$ (mJy) ±10%	$S_{10\,GHz}$ (mJy) ±10%	$S_{11\,GHz}$ (mJy) ±10%	$\theta_s(X)$ ("×")	$S_{Peak}(K)$ (mJy/beam) ±10%	$\sigma(K)$ (mJy)	$S_{20\,GHz}$ (mJy) ±10%	$S_{22\,GHz}$ (mJy) ±10%	$S_{24\,GHz}$ (mJy) ±10%	$\theta_s(K)$ ("×")
(1)	(2)	(3)	(4)	(5)	(6)	(7)	(8)	(9)	(10)	(11)	(12)	(13)
G010.3009−00.1477⊕	88.1	3.1	700.3	686.7	661.4	6.8×6.6	15.9	0.7	433.4	419.6	392.6	6.5×6.4
G010.4724+00.0275	82.5	1.6	100.7	105.9	115.4	1.4×0.4	66.9	0.8	156.8	159.9	172.0	1.6×0.5
G010.6234−00.3837⊕	1099.9	7.9	3071.4	3072.1	3314.8	4.2×3.8	572.3	14.6	2884.8	2857.2	2851.5	3.1×3.0
G010.9584+00.0221	186.3	1.5	258.3	256.2	265.0	1.2×0.9	91.3	1.2	210.7	202.6	200.6	1.0×0.7
G011.0328+00.0274	3.9	0.2	4.8	4.3	4.1	1.3×0.9	1.7	0.1	3.4	2.9	2.8	0.9×0.4
G011.1104−00.3985⊕	70.5	0.7	350.4	334.8	327.7	9.5×9.4	15.6	0.4	136.1	123.3	126.1	2.2×1.7
G011.1712−00.0662⊕	4.1	0.1	95.1	92.7	100.1	11.9×8.6	0.6	0.1	–	–	–	–
G011.9368−00.6158⊕	306.7	2.0	1116.4	1083.5	1098.3	3.4×3.2	76.4	2.0	656.1	652.4	629.6	2.8×1.8
G011.9446−00.0369⊕	85.7	2.0	709.6	691.4	724.6	6.3×4.7	20.0	0.6	307.2	291.6	289.9	4.3×2.1
G012.1988−00.0345	29.6	0.4	66.0	64.8	63.9	2.0×1.9	6.5	0.2	59.6	54.7	55.9	2.0×2.0
G012.2081−00.1019	88.0	0.8	212.5	209.3	206.5	2.3×1.9	27.2	0.6	159.0	142.1	140.8	2.0×1.2
G012.4294−00.0479	19.9	0.4	51.7	49.8	49.8	2.8×2.4	6.6	0.2	28.0	22.9	26.9	1.7×0.9
G012.8050−00.2007⊕	858.6	11.0	16097.6	15749.0	16931.9	17.1×17.0	302.3	4.9	6400.9	6240.9	6252.3	8.1×1.1
G012.9995−00.3583	8.4	0.1	14.6	14.7	15.0	1.9×1.1	3.3	0.1	12.4	11.1	11.2	1.8×0.8
G013.2099−00.1428⊕	57.4	0.4	1080.7	1065.6	965.8	11.7×11.6	10.7	0.3	385.9	359.6	354.2	9.0×9.0
G013.3850+00.0684⊕	15.0	0.6	738.1	819.3	812.9	21.3×21.2	1.6	0.1	–	–	–	–
G014.7785−00.3328	18.9	0.2	25.3	25.0	25.4	1.1×0.8	9.7	0.1	17.7	16.3	15.9	0.7×0.5
G016.1448+00.0088	13.7	0.1	16.6	16.6	16.6	0.9×0.8	7.7	0.1	14.3	13.4	13.0	0.7×0.5
G016.3913−00.1383⊕	2.5	0.1	50.0	52.5	46.9	9.9×8.1	0.4	0.1	31.9	21.0	22.9	7.0×4.6
G016.9445−00.0738⊕	138.3	0.4	545.2	548.9	546.6	3.5×2.5	30.6	0.3	529.2	513.4	515.6	3.5×2.7
G017.0299−00.0696	2.7	0.1	3.9	3.8	3.9	1.6×0.5	1.1	0.1	1.9	2.1	3.1	0.8×0.5
G017.1141−00.1124	4.9	0.1	16.5	15.9	16.3	3.1×2.5	1.0	0.1	10.3	8.2	11.5	2.5×1.6
G018.3024−00.3910⊕	56.9	0.7	1281.9	1308.6	1180.6	15.5×13.3	12.7	1.0	–	–	–	–
G018.4433−00.0056	38.2	2.6	73.0	73.9	95.3	1.8×1.5	6.3	0.7	72.4	57.4	76.1	2.2×1.8
G018.4614−00.0038	178.6	0.8	387.2	383.5	394.4	2.1×1.8	54.0	0.9	355.7	322.1	388.6	2.1×1.6
G018.6654+00.0294	4.9	0.8	6.9	6.7	6.6	1.7×1.4	2.5	0.1	5.3	5.4	5.5	0.8×0.7
G018.7106+00.0002	88.5	0.5	116.9	116.2	116.0	1.1×0.9	42.5	0.4	104.2	101.2	100.8	0.9×0.8
G018.7612+00.2630	42.6	0.2	55.7	55.3	55.4	1.1×0.9	18.9	0.2	45.6	47.6	50.4	0.9×0.8
G018.8250−00.4675	4.4	0.1	10.2	9.9	10.5	2.5×2.2	1.2	0.1	8.3	6.3	7.7	1.6×1.5
G018.8338−00.3002⊕	56.0	0.5	132.6	135.2	139.0	5.8×5.6	52.8	0.3	65.9	66.4	65.1	0.4×0.3
G019.0754−00.2874⊕	19.5	0.7	369.2	326.8	355.5	15.2×15.2	6.5	0.5	–	–	–	–
G019.4912+00.1352⊕	23.1	0.4	355.3	374.2	417.1	9.6×8.1	5.0	0.3	176.0	151.5	196.4	5.9×4.4
G019.6087−00.2351⊕	249.2	3.5	3535.0	3145.6	3497.1	14.0×13.9	45.6	1.0	–	–	–	–
G019.6090−00.2313	255.4	3.0	247.0	259.8	241.0	3.1×1.1	50.1	1.5	130.0	133.0	145.9	1.4×0.6
G019.7407−00.2821⊕	3.6	0.1	166.4	168.5	167.7	21.3×21.2	0.6	0.1	–	–	–	–
G019.7549−00.1282	40.3	0.4	44.6	44.5	44.8	0.6×0.5	29.8	0.5	40.8	40.1	39.1	0.5×0.4
G020.0809−00.1362	205.7	2.3	645.7	656.2	696.5	3.8×1.6	188.7	1.6	387.0	381.0	400.0	1.0×0.5
G020.3633−00.0136	17.6	0.3	53.8	53.2	52.4	2.8×2.3	3.9	0.1	45.9	46.6	47.5	2.8×2.3
G021.3571−00.1766	16.7	0.3	25.4	25.1	24.7	1.4×1.1	6.9	0.1	22.7	21.1	23.8	1.2×1.1
G021.3855−00.2541	81.2	0.4	122.8	121.4	120.8	1.4×1.0	39.5	0.1	103.9	101.7	108.8	1.1×0.9
G021.4257−00.5417⊕	2.3	0.2	72.7	75.0	71.1	11.8×10.6	0.4	0.1	–	–	–	–
G023.2654+00.0765⊕	20.1	0.2	83.3	85.6	82.8	5.3×5.0	5.5	0.2	47.7	43.1	46.7	2.7×1.5
G023.4553−00.2010	13.7	0.5	13.8	12.9	10.9	1.2×0.8	11.0	0.1	13.9	13.5	13.2	0.3×0.3
G024.5065−00.2224⊕	19.9	0.7	257.0	249.5	258.1	7.7×7.5	4.6	0.2	127.3	119.0	117.5	5.2×5.1
G024.7889+00.0824†	25.6	1.1	33.1	37.8	35.7	1.9×1.1	6.9	0.8	23.7	22.9	20.1	1.4×1.2
G024.7898+00.0833	32.4	1.1	31.6	32.9	30.8	1.4×0.9	65.0	0.8	65.8	72.3	71.2	0.3×0.2
G025.3948+00.0332	35.9	0.9	367.9	358.2	369.9	5.1×4.9	7.4	0.4	318.9	278.8	303.5	4.7×4.4
G025.3970+00.5614	117.8	0.7	158.5	164.8	163.1	1.3×0.7	71.4	0.6	158.5	153.5	161.3	0.8×0.8
G025.3981−00.1411⊕	180.3	3.8	2444.6	2668.5	2510.9	7.5×7.5	36.0	2.7	711.0	734.0	725.0	4.7×4.7
G025.7157+00.0487	12.4	0.2	20.8	21.3	22.5	1.5×1.4	3.9	0.2	15.8	15.8	18.0	1.4×1.1
G025.8011−00.1568	26.6	0.2	37.1	36.8	36.3	1.1×1.0	10.9	0.1	33.9	32.2	33.3	1.1×1.0
G026.5444+00.4169⊕	15.3	1.0	532.2	556.4	598.7	17.4×17.3	2.5	0.3	–	–	–	–
G027.2800+00.1447⊕	46.0	0.6	433.7	466.2	446.7	6.0×5.1	9.6	0.6	357.2	289.2	302.8	5.6×3.7
G027.3644−00.1657	37.0	0.2	58.5	56.7	55.8	1.4×1.1	14.9	0.2	40.1	38.4	40.7	0.9×0.8
G027.9782+00.0789⊕	5.5	0.2	125.3	127.0	144.8	12.9×12.8	0.7	0.1	–	–	–	–
G028.2003−00.0494	259.6	1.8	298.0	320.0	339.0	0.9×0.6	339.1	2.1	558.0	582.0	627.0	0.7×0.5
G028.2879−00.3641	123.9	1.2	592.7	581.1	601.7	4.0×3.8	42.5	1.3	614.6	577.6	549.7	2.1×1.0
G028.6082+00.0185⊕	52.2	1.1	226.4	228.7	242.5	3.4×3.1	14.7	0.3	188.0	173.0	190.8	3.1×2.4
G029.9559−00.0168⊕	357.2	7.5	2667.2	2826.8	2951.5	5.9×4.2	103.2	2.4	1519.0	1353.6	1502.1	4.4×1.8
G030.0096−00.2734	5.6	0.1	5.7	5.8	5.8	0.3×0.2	4.9	0.1	5.8	5.5	5.3	0.2×0.2
G030.5353+00.0204⊕	103.9	1.3	684.7	676.5	682.7	6.7×6.7	25.1	0.8	379.7	380.5	391.2	5.0×5.0
G031.0495+00.4697	10.4	0.1	13.5	13.4	13.1	1.2×0.7	3.4	0.1	12.5	11.7	13.1	1.3×0.8
G031.1596+00.0448	18.6	0.1	24.9	24.7	24.4	1.1×0.9	7.1	0.1	20.6	19.1	20.4	0.9×0.8
G031.2801+00.0632⊕	14.3	0.6	353.0	400.1	416.5	10.9×10.2	2.1	0.3	–	–	–	–

Table A.2. –continuue Observation results of 112 young H II regions at X-band (8–12 GHz) and K-band (18–26 GHz).

Name	$S_{\text{Peak}}(X)$ (mJy/beam)	$\sigma(X)$ (mJy)	$S_{9\,\text{GHz}}$ (mJy) ±10%	$S_{10\,\text{GHz}}$ (mJy) ±10%	$S_{11\,\text{GHz}}$ (mJy) ±10%	$\theta_s(X)$ ($''\times''$)	$S_{\text{Peak}}(K)$ (mJy/beam) ±10%	$\sigma(K)$ (mJy)	$S_{20\,\text{GHz}}$ (mJy) ±10%	$S_{22\,\text{GHz}}$ (mJy) ±10%	$S_{24\,\text{GHz}}$ (mJy) ±10%	$\theta_s(K)$ ($''\times''$)
(1)	(2)	(3)	(4)	(5)	(6)	(7)	(8)	(9)	(10)	(11)	(12)	(13)
G032.4727+00.2036	60.1	0.2	102.4	101.1	100.1	1.5×1.2	24.2	0.2	86.7	82.2	85.7	1.4×0.9
G032.7441−00.0755	15.1	0.1	16.2	17.3	18.8	1.0×0.7	31.4	0.1	29.8	31.8	34.7	0.1×0.1
G032.7966+00.1909⊕	623.5	6.2	3768.0	3813.0	3925.0	11.5×11.4	238.8	6.1	–	–	–	–
G032.9273+00.6060⊕	54.3	0.5	278.5	272.8	284.5	7.6×7.6	25.1	0.2	–	–	–	–
G033.4163−00.0036⊕	7.0	0.3	111.5	98.4	101.8	10.1×9.9	1.1	0.1	30.5	18.5	20.9	3.8×2.2
G033.9145+00.1105⊕	121.2	1.9	732.4	737.6	740.7	6.0×6.0	31.5	0.7	270.9	263.9	288.9	2.8×1.4
G034.2572+00.1535⊕	956.0	11.0	2710.0	2970.0	3050.0	2.9×1.9	648.0	5.5	3750.0	3760.0	4200.0	1.8×1.2
G034.2573+00.1523†	117.0	10.8	145.6	141.5	180.0	1.7×0.6	60.7	7.5	57.0	45.4	33.1	0.6×0.6
G034.2581+00.1533	182.0	11.4	101.7	110.5	116.9	1.8×1.4	88.0	10.0	120.0	120.0	169.0	0.4×0.2
G034.4032+00.2277	7.7	0.1	9.0	8.9	8.7	0.8×0.5	5.1	0.1	6.9	7.0	6.9	0.4×0.4
G035.0242+00.3502	12.0	0.1	13.1	13.0	13.0	0.8×0.6	9.6	0.1	11.8	11.9	12.2	0.3×0.3
G035.4669+00.1394⊕	34.3	0.3	309.0	288.0	301.0	6.3×6.1	6.9	0.4	163.0	148.0	173.5	4.6×3.5
G035.5781−00.0305	141.1	0.7	218.2	202.8	212.1	1.3×0.9	147.7	1.1	209.2	202.0	207.6	0.6×0.2
G036.4057+00.0226	15.4	0.45	23.5	23.6	24.1	2.3×1.6	4.4	0.32	18.9	18.9	19.6	1.4×1.3
G036.4062+00.0221†	10.4	0.45	11.4	11.3	10.5	2.3×1.7	7.8	0.32	8.1	7.7	7.9	1.9×1.7
G037.5457−00.1120⊕	38.7	1.0	450.0	499.0	550.0	7.0×5.5	8.4	0.4	167.8	142.3	168.8	3.5×2.8
G037.7347−00.1128	12.9	0.2	16.3	16.3	16.7	1.1×0.9	6.1	0.1	14.6	13.9	14.4	0.8×0.7
G037.8731−00.3996⊕	552.8	7.0	2588.0	2465.0	2720.0	4.1×3.5	264.1	3.5	1320.0	1201.0	1153.0	1.2×1.1
G037.9723−00.0965	9.2	0.1	21.0	21.5	20.5	1.9×1.9	2.5	0.1	18.9	17.0	20.6	1.9×1.7
G038.8756+00.3080	89.4	0.7	305.2	295.2	318.1	2.8×2.5	22.8	0.8	231.9	210.5	238.2	2.2×1.9
G039.1956+00.2255	48.4	0.2	62.0	60.6	60.6	0.8×0.8	22.6	0.3	58.3	56.7	55.8	0.8×0.8
G039.8824−00.3460⊕	65.8	0.4	367.4	361.7	373.8	3.8×3.5	14.7	0.6	214.5	212.0	226.4	3.2×3.2
G042.4345−00.2605⊕	23.4	0.4	66.2	62.7	61.3	3.1×2.7	6.0	1.2	42.3	40.0	41.4	2.7×1.4
G043.1651−00.0283⊕	544.9	13.5	3809.0	3607.1	4020.7	7.6×7.5	215.6	4.5	2023.9	1941.5	–	3.4×3.3
G043.1652+00.0129	286.0	17.1	310.0	326.0	338.2	1.7×1.4	345.0	10.5	529.0	545.0	516.0	0.6×0.4
G043.1657+00.0116	271.0	16.4	370.6	381.7	416.0	2.4×1.8	132.0	13.1	–	–	–	–
G043.1665+00.0106⊕	524.4	18.0	2740.0	2766.6	2900.0	3.6×3.2	292.9	11.4	2257.4	2068.0	2293.9	2.9×2.8
G043.1778−00.5181	12.9	0.5	150.2	146.4	160.0	6.9×6.9	1.8	0.3	39.5	40.3	41.0	4.3×2.8
G045.0694+00.1323	35.4	1.7	71.0	78.0	80.0	1.8×1.8	448.1	4.2	–	–	–	–
G045.0712+00.1321	–	1.3	388.0	424.0	461.2	0.8×0.6	436.5	4.2	750.0	745.0	806.5	0.6×0.5
G045.1223+00.1321⊕	831.8	5.4	4191.0	4036.4	4197.0	12.8×12.7	517.5	5.7	2860.1	2847.0	2888.9	2.7×2.6
G045.4545+00.0591⊕	79.2	6.6	940.0	1057.0	1020.0	8.8×8.7	12.5	1.0	194.0	177.0	162.0	6.2×6.1
G045.4656+00.0452	109.7	2.5	135.6	139.2	134.0	1.2×0.5	93.2	0.1	139.4	155.5	143.0	0.8×0.4
G045.4790+00.1294⊕	17.0	2.6	326.0	304.0	349.3	8.6×8.4	0.4	0.1	–	–	–	–
G048.6057+00.0228	28.1	0.3	44.5	47.6	44.3	1.8×1.3	9.6	0.3	31.6	29.8	32.0	0.9×0.9
G048.6099+00.0270⊕	27.8	0.6	98.2	97.1	102.0	6.9×6.8	0.4	0.6	–	–	–	–
G048.9296−00.2793⊕	15.0	1.6	316.0	283.0	311.2	9.2×8.1	1.2	1.6	32.1	29.9	30.2	3.6×3.6
G049.2679−00.3374⊕	6.5	0.4	72.2	71.0	81.3	5.1×5.0	1.1	0.2	32.7	28.6	35.6	3.2×3.2
G049.3666−00.3010†	54.0	4.9	387.0	367.3	406.7	6.4×6.2	1.0	1.3	–	–	–	–
G049.3704−00.3012	54.8	4.9	652.4	646.0	667.0	9.1×9.0	5.5	1.3	269.0	177.0	152.5	4.8×3.8
G049.4905−00.3688⊕	667.2	9.9	3900.0	3770.0	4020.0	3.9×3.7	186.7	8.2	2591.4	2336.9	2470.8	2.8×2.8
G050.3152+00.6762	47.1	0.4	79.6	76.8	76.1	1.3×1.2	15.9	0.2	62.7	59.4	63.9	1.3×1.0
G051.6785+00.7193	27.4	0.1	30.7	31.2	32.4	1.1×0.5	33.9	0.2	35.0	35.8	38.2	0.2×0.1
G052.7533+00.3340⊕	17.1	0.2	370.2	368.6	371.6	8.9×8.0	2.1	0.3	–	–	–	–
G053.9589+00.0320	20.5	0.1	45.3	44.6	43.5	1.8×1.6	5.7	0.2	35.0	31.8	38.2	1.7×1.2
G060.8842−00.1286	24.1	0.8	34.1	36.2	32.6	1.7×1.5	11.1	0.2	24.9	23.3	24.2	0.7×0.7
G061.4763+00.0892⊕	129.2	3.5	580.4	550.0	592.1	4.5×4.3	56.8	1.5	334.0	324.0	400.0	3.5×2.0
G061.4770+00.0892†	125.0	3.5	153.0	155.0	161.0	1.61×1.0	29.0	1.5	137.5	127.9	157.0	0.9×0.6

Notes. † refers to the added 5 UC H II regions in the observed fields with rising spectra between C and X band, see Sect 3.1. ⊕ indicates that the sources are extended and their K-band flux densities should be considered to be lower limits. Columns: (1) Source name; (2) and (3) peak flux density and local RMS at X-band; (4-6) flux density at 9 GHz, 10 GHz and 11 GHz, respectively; (7) deconvolved source size at X-band; (8) and (9) peak flux density and RMS at K-band; (10-12) flux density at 20 GHz, 22 GHz and 24 GHz, respectively; (13) deconvolved source size at K-band. The symbol of ±10% refers to an overall estimation of the percentage error at each frequency.

**Table A.3.** Derived physical properties of 116 young H II regions.

Name	n_e	$diam$	EM	ν_t	$\log N_{Ly}$	Spectral	f_d
	(10^5 cm^{-3})	(pc)	(10^7 pc cm^{-6})	(GHz)	(s^{-1})	Type	
(1)	(2)	(3)	(4)	(5)	(6)	(7)	(8)
G010.3009−00.1477	0.09	0.119	0.92	1.69	47.94	O9.5	0.86
G010.4724+00.0275	1.43	0.022	45.2	10.77	48.11	O9	0.94
G010.6234−00.3837	0.16	0.166	4.39	3.55	48.9	O6.5	0.81
G010.9584+00.0221	0.36	0.029	3.78	3.31	47.35	B0	−
G011.0328+00.0274	0.13	0.014	0.24	0.89	45.57	B1	−
G011.1104−00.3985	0.07	0.145	0.62	1.4	47.94	O9.5	0.27
G011.1712−00.0662	0.09	0.053	0.45	1.21	46.91	B0	−
G011.9368−00.6158	0.07	0.155	0.86	1.63	48.12	O9	0.19
G011.9446−00.0369	0.17	0.075	2.2	2.56	47.84	O9.5	−
G012.1988−00.0345	0.07	0.148	0.65	1.43	47.98	O9	0.77
G012.2081−00.1019	0.05	0.268	0.72	1.5	48.59	O7	0.83
G012.4294−00.0479	0.26	0.02	1.38	2.05	46.55	B0.5	−
G012.8050−00.2007	0.1	0.248	2.68	2.81	49.05	O6	−
G012.9995−00.3583	0.28	0.008	0.6	1.38	45.41	B1	−
G013.2099−00.1428	0.14	0.082	1.67	2.24	47.88	O9.5	−
G013.3850+00.0684	0.37	0.032	4.43	3.57	47.49	B0	−
G014.7785−00.3328	0.27	0.016	1.21	1.92	46.4	B0.5	−
G016.1448+00.0088	0.14	0.058	1.11	1.85	47.42	B0	−
G016.3913−00.1383	0.16	0.023	0.59	1.36	46.3	B0.5	−
G016.9445−00.0738	0.06	0.389	1.48	2.12	49.16	O6	−
G017.0299−00.0696	0.2	0.024	0.94	1.7	46.61	B0.5	−
G017.1141−00.1124	0.03	0.145	0.1	0.59	47.23	B0	0.75
G018.3024−00.3910	0.07	0.158	0.83	1.61	48.15	O8.5	0.14
G018.4433−00.0056	0.07	0.16	0.68	1.46	48.04	O9	−
G018.4614−00.0038	0.11	0.196	2.23	2.57	48.75	O6.5	0.54
G018.6654+00.0294	0.17	0.034	1.01	1.76	46.92	B0	0.88
G018.7106+00.0002	0.3	0.023	2.03	2.46	46.84	B0	−
G018.7612+00.2630	0.11	0.111	1.36	2.03	48.05	O9	0.83
G018.8250−00.4675	0.05	0.051	0.13	0.66	46.41	B0.5	−
G018.8338−00.3002	0.05	0.251	0.55	1.32	48.36	O8	0.29
G019.0754−00.2874	0.06	0.205	0.33	1.04	47.99	O9	0.85
G019.4912+00.1352	0.04	0.388	0.77	1.55	48.87	O6.5	−
G019.6087−00.2351	0.09	0.416	3.06	2.99	49.5	O5	0.63
G019.6090−00.2313	0.08	0.219	1.34	2.02	48.63	O6.5	0.95
G019.7407+00.2821	0.15	0.138	3.13	3.02	48.54	O7.5	−
G019.7549−00.1282	0.29	0.037	3.17	3.04	47.45	B0	0.59
G020.0809−00.1362	0.14	0.191	3.49	3.18	49.04	O6	0.52
G020.3633−00.0136	0.17	0.032	0.96	1.73	46.81	B0	−
G021.3571−00.1766	0.13	0.062	1.02	1.77	47.42	B0	0.62
G021.3855−00.2541	0.12	0.108	1.61	2.21	48.1	O9	0.61
G021.4257−00.5417	0.04	0.091	0.17	0.77	46.98	B0	0.58
G023.2654+00.0765	0.11	0.073	0.87	1.65	47.49	B0	−
G023.4553−00.2010	0.49	0.015	3.55	3.21	46.72	B0.5	−
G024.5065−00.2224	0.08	0.118	0.91	1.68	47.94	O9.5	0.46
G024.7889+00.0824	0.25	0.031	1.94	2.41	47.21	B0	0.92
G024.7898+00.0833	3.38	0.008	91.84	15.1	47.52	B0	0.92
G025.3948+00.0332	0.05	0.36	1.01	1.76	48.96	O6	0.24
G025.3970+00.5614	0.07	0.211	1.08	1.82	48.52	O7.5	0.20
G025.3981−00.1411	0.04	0.589	1.17	1.89	49.46	O5.5	0.66
G025.7157+00.0487	0.09	0.071	0.54	1.31	47.29	B0	0.72
G025.8011−00.1568	0.13	0.07	1.23	1.94	47.6	O9.5	0.87
G026.5444+00.4169	0.06	0.271	1.04	1.79	48.75	O6.5	0.15
G027.2800+00.1447	0.03	0.505	0.49	1.26	48.94	O6.5	−
G027.3644−00.1657	0.05	0.12	0.35	1.06	47.58	B0	0.83
G027.9782+00.0789	0.1	0.078	0.78	1.56	47.49	B0	−
G028.2003−00.0494	1.41	0.027	53.54	11.68	48.37	O8	0.43
G028.2879−00.3641	0.05	0.398	0.81	1.59	48.91	O6.5	0.80
G028.6082+00.0185	0.06	0.17	0.68	1.46	48.12	O9	0.60
G029.9559−00.0168	0.06	0.331	1.14	1.87	48.9	O6.5	0.65
G030.0096−00.2734	1.91	0.004	15.57	6.49	46.21	B0.5	−

Table A.3. –continuue Derived physical properties of 116 young H II regions.

Name	n_e	*diam*	EM	ν_t	$\log N_{Ly}$	Spectral	f_d
	$(10^5\,\mathrm{cm}^{-3})$	(pc)	$(10^7\,\mathrm{pc\,cm}^{-6})$	(GHz)	(s^{-1})	Type	
(1)	(2)	(3)	(4)	(5)	(6)	(7)	(8)
G030.5353+00.0204	0.07	0.12	0.55	1.32	47.73	O9.5	−
G030.5887−00.0428	2.08	0.009	39.1	10.06	47.28	B0	−
G030.7197−00.0829	0.22	0.093	4.54	3.61	48.44	O7.5	−
G030.8662+00.1143	0.37	0.031	4.25	3.5	47.46	O9.5	−
G031.0495+00.4697	0.21	0.012	0.56	1.34	45.75	B1	−
G031.1596+00.0448	0.12	0.026	0.39	1.13	46.27	B0.5	−
G031.2801+00.0632	0.14	0.092	1.78	2.31	48.05	O9	0.49
G032.4727+00.2036	0.19	0.033	1.25	1.96	46.98	B0	−
G032.7441−00.0755	2.79	0.011	82.77	14.37	47.69	O9.5	0.88
G032.7966+00.1909	0.04	0.81	1.5	2.13	49.83	O4	0.21
G032.9273+00.6060	0.03	0.44	0.52	1.29	48.83	O6.5	−
G033.1328−00.0923	0.21	0.1	4.56	3.61	48.54	O7.5	0.16
G033.4163−00.0036	0.12	0.066	1.01	1.76	47.48	B0	−
G033.9145+00.1105	0.07	0.229	0.98	1.74	48.57	O8	0.44
G034.2572+00.1535	0.52	0.038	10.12	5.28	48.03	O9	0.51
G034.2573+00.1523	3.55	0.005	58.23	12.16	46.58	B0.5	0.98
G034.2581+00.1533	3.01	0.004	37.26	9.83	46.54	B0.5	0.98
G034.4032+00.2277	0.38	0.006	0.87	1.65	45.38	B1	−
G035.0242+00.3502	0.47	0.008	1.74	2.28	45.86	B0.5	0.58
G035.4669+00.1394	0.05	0.24	0.6	1.37	48.33	O8	0.82
G035.5781−00.0305	0.22	0.093	4.46	3.58	48.36	O8	0.81
G036.4057+00.0226	0.33	0.016	1.74	2.29	46.48	B0.5	−
G036.4062+00.0221	0.13	0.022	0.4	1.13	46.16	B0.5	−
G037.5457−00.1120	0.07	0.242	1.23	1.94	48.7	O7	0.24
G037.7347−00.1128	0.1	0.062	0.62	1.4	47.21	B0	0.77
G037.8731−00.3996	0.05	0.532	1.41	2.07	49.38	O5.5	0.42
G037.9723−00.0965	0.13	0.082	1.36	2.03	47.79	O9.5	−
G038.8756+00.3080	0.05	0.344	0.74	1.52	48.79	O6.5	−
G039.1956+00.2255	0.2	0.081	3.26	3.08	48.12	O9	−
G039.8824−00.3460	0.05	0.256	0.7	1.48	48.51	O7.5	−
G042.4345−00.2605	0.15	0.044	1.06	1.8	47.1	B0	−
G043.1651−00.0283	0.12	0.387	5.33	3.9	49.69	O5	0.42
G043.1652+00.0129	0.88	0.053	41.47	10.34	48.91	O6.5	0.90
G043.1657+00.0116	1.57	0.046	113.18	16.68	48.69	O7	0.94
G043.1665+00.0106	0.24	0.22	12.21	5.78	49.55	O5	0.58
G043.1778−00.5181	0.06	0.165	0.58	1.36	48.11	O9	0.71
G045.0694+00.1323	0.74	0.026	13.97	6.16	47.76	O9.5	0.97
G045.0712+00.1321	1.22	0.04	58.98	12.23	48.73	O6.5	0.76
G045.1223+00.1321	0.07	0.429	2.08	2.49	49.43	O5.5	0.68
G045.4545+00.0591	0.08	0.235	1.4	2.06	48.72	O6.5	0.77
G045.4656+00.0452	1.02	0.023	23.56	7.89	47.88	O9.5	0.81
G045.4790+00.1294	0.01	0.462	0.09	0.56	48.06	O9	−
G048.6057+00.0228	0.31	0.042	4.1	3.44	47.76	O9.5	0.97
G048.6099+00.0270	0.1	0.116	1.19	1.91	47.99	O9	0.85
G048.9296−00.2793	0.22	0.065	3.26	3.08	47.97	O9	−
G049.2679−00.3374	0.07	0.089	0.49	1.25	47.46	B0	−
G049.3666−00.3010	0.94	0.031	26.89	8.41	48.05	O9	0.83
G049.3704−00.3012	0.11	0.128	1.61	2.2	48.34	O8	0.67
G049.4905−00.3688	0.1	0.27	2.57	2.75	49.04	O6	0.85
G050.3152+00.6762	0.26	0.018	1.2	1.92	46.42	B0.5	−
G051.6785+00.7193	0.64	0.026	10.74	5.44	47.68	O9.5	0.88
G052.7533+00.3340	0.05	0.254	0.75	1.53	48.51	O7.5	−
G053.9589+00.0320	0.06	0.066	0.24	0.89	46.87	B0	−
G060.8842−00.1286	0.93	0.012	10.8	5.35	46.4	B0.5	−
G061.4763+00.0892	0.13	0.09	1.72	2.27	48.1	O9	0.81
G061.4770+00.0892	4.45	0.004	78.76	14.04	46.81	B0	0.99

Notes. The fraction of Lyman continuum photons absorbed by dust within H II regions f_d should be taken as upper limits. The Symbol − means no measurement. Columns: (1) source name; (2) electron density; (3) physical diameter; (4) emission measure; (5) turnover frequency; (6) Lyman continuum flux; (7) spectral type; (8) dust absorption fraction.

Appendix B: The SED fitting for the young H II regions and their images in C-band (CORNISH), and in X-band and K-band (this work)

(a) Radio SED   (b) C-band image   (c) X-band image   (d) K-band image
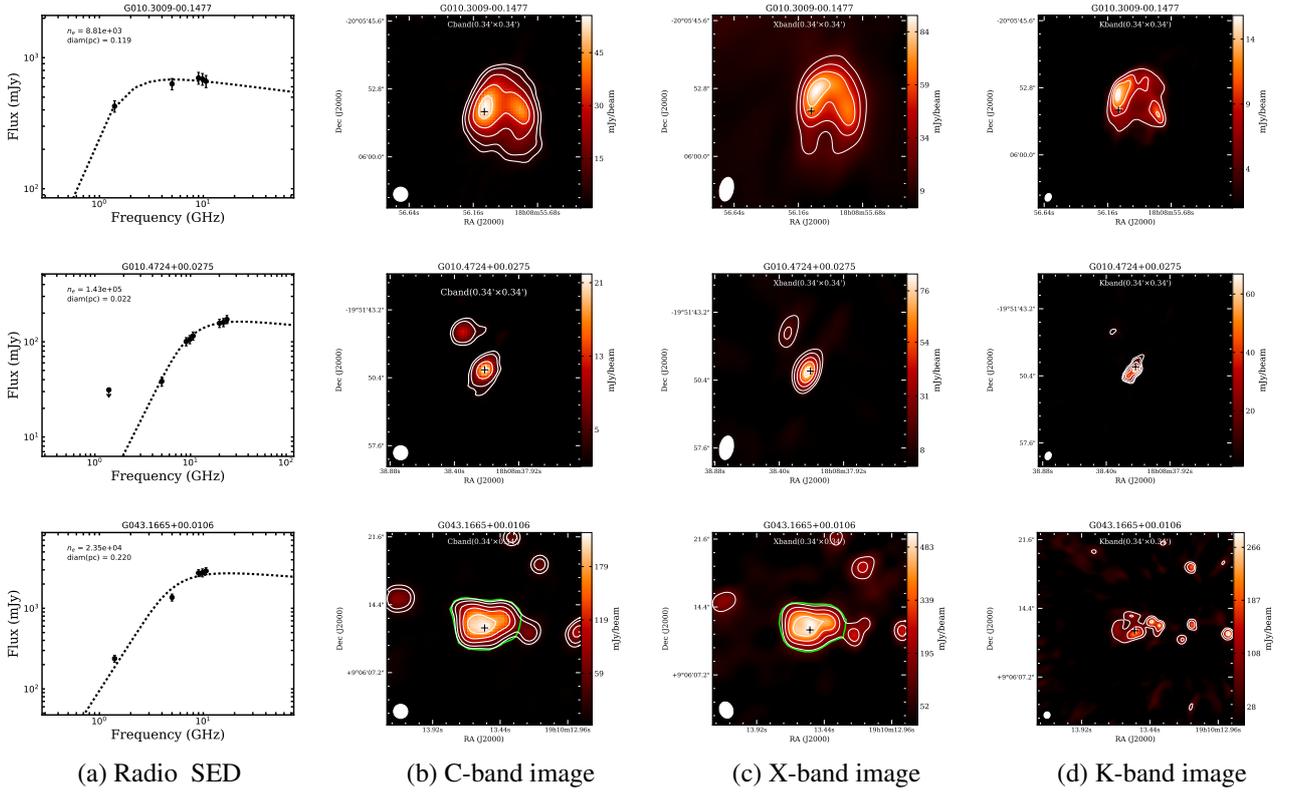
Fig. B.1. The examples of the best-fitting SEDs and the radio images in C-band (CORNISH), X-band and K-band observations (this work). Figures for the full sample is given in the additional file named "summary-images-and-fitting-results-for-the-sample.pdf", and will be available in electronic form at the CDS. (a) the radio spectral energy distribution (SED) and best-fitting model for each source in the sample. The SED shows the free-free emission fit to flux density points between 1 and 26 GHz for a single compact source, while the extended source has the best fit to flux density points between 1 and 11 GHz as their K-band flux measurements are not reliable owing to the shortage of short baseline spacings. The uncertainties of flux measurements of these points are used to constrain the fitting process and to obtain the best estimate. The best-fitting results of electron density $n_e (cm^{-3})$ and physical diameter *diam* (pc) for each source are shown in the upper-left corner of each figure. (b), (c) and (d) the radio images in C-band, X-band, and K-band marked with the positions of the young UC H II regions in each image, including single component compact sources, extended sources, cluster sources. The C-band images have been taken from the CORNISH survey and have been used to compare with the images at X-band in this work as the X-band observations have comparable beam sizes as the CORNISH survey. For some sources, the K-band images are not shown due to the bad quality of observational data at K-band. The lime polygons in the C-band images shown for some sources are similar to the defined region in the CORNISH survey. The lime polygons in the X-band images shown for some sources refer to the manually drawn emission regions to measure the observational results following the same strategy in CORNISH survey. The white contour levels in the image are equally spaced by 5σ and starting at a level of 5σ. The image size of each target is shown in the upper-middle of each image. The beam sizes for C-band (1.5″), X-band (∼ 1.7″), and K-band (0.7″) are shown in the lower-left corner of each image.